Application of Nanostructures in

Thermal Emission, Photon Management and Spectral Sensing

by

Zhu Wang

A dissertation submitted in partial fulfillment
of the requirements for the degree of

DOCTOR OF PHILOSOPHY

(Electrical and Computer Engineering)

at the

University of Wisconsin Madison

2018

Date of final oral examination: July 12 2018

The dissertation is approved by the following members of the Final Oral Committee:

Mikhail Kats, Professor, Electrical and Computer Engineering
Ting Shan Luk, Scientist, Sandia National Laboratories
Zhenqiang Ma, Professor, Electrical and Computer Engineering
Zongfu Yu, Professor, Electrical and Computer Engineering

Application of Nanostructures in Thermal Emission, Photon Management and Spectral Sensing

Zhu Wang

Under the supervision of Professor Zongfu Yu

At the University of Wisconsin Madison

Abstract

Nanostructures have attracted great interest in recent years as they display quite different characteristics from their bulk behavior. The applications of nanostructures, including thin films and photonic crystal slabs, are explored in the field of thermal emission, photon management and spectral sensing.

Infrared thermal emission from metals has important energy applications in thermophotovoltaics, radiative cooling, and lighting. Unfortunately, the emissivity of flat metal films is close to zero because the screening effect prevents metals' fluctuating currents from emitting to the far field. As a result, metal films are often used as reflecting mirrors instead of thermal emitters. Recently, nanostructured metals, such as metamaterials, have emerged as an interesting way to enhance and to spectrally control thermal emission based on plasmonic resonant effects. However, they require sophisticated lithography. Here, a completely different mechanism to achieve spectrally selective metallic emitters based on a tunneling effect is

proposed and experimentally demonstrated. This effect allows a simple flat metal film to achieve a near-unity emissivity with controlled spectral selectivity for efficient heat-to-light energy conversion.

Index-near-zero thin films can be used for effective photon management. They help to restrict the angle of acceptance, resulting in greatly enhanced light trapping limit. In addition, these materials also decrease the radiative recombination, leading to enhanced open circuit voltage and energy efficiency in direct bandgap solar cells.

A method of spectral sensing based on compressive sensing is shown to have the potential to achieve high resolution in a compact device size. The random bases used in compressive sensing are created by the optical response of a set of different nanophotonic structures, such as photonic crystal slabs. The complex interferences in these nanostructures offer diverse spectral features suitable for compressive sensing.

Acknowledgements

First, the author would like to thank her research advisor, professor Zongfu Yu, for providing the opportunity to perform research in his lab, and for all his guidance and advices. The author also wishes to thank her thesis defense committee members, Professor Mikhail Kats, Professor Zhenqiang Ma, and Dr. Ting Shan Luk, for their valuable comments and suggestions.

The author acknowledgements her coworkers for their contributions to this thesis. Ting Shan Luk, Tony James and John Nogan helped with device fabrication and characterization. Professor Qiaoqiang Gan and one of his students, Denxin Ji measured the thermal emission spectrum. Ming Zhou, helped with the simulation for calculating thermal emission of a point source in COMSOL. Chun-Chieh Chang contributed to the fabrication recipe development for the micro-spectrometer. Soongyu Yi helped with the device characterization and measurement setup. Professor Mikhail Kats, together with two of his students, Graham Joe, Alireza Shahsafi, performed some FTIR measurements for the fabricated device. The author also got support from Erfan Khoram, Ang Chen and Yixuan Tan, for device characterization and coding. In addition, the author would like to thank Professor Yuerui Lu, and two of his students Jiong Yang and Linglong Zhang, to provide the opportunity to work with them in the field of 2D materials, which is not covered in the thesis.

Finally, the author would like to thank her family and friends, for their unconditional support and encouragements over the years.

Table of Contents

List of Figures

CHAPTER ONE

INTRODUCTION

1.1 Background

Devices with nanostructures have been developed over years to confine, control and guide light [1]. A key motivation for the development of nanostructure devices is that structures with reduced dimensions display quite different characteristics from their bulk behavior. Due to quantum effect, properties of nanoscale materials and devices, such as melting point [2], electrical conductivity [3], permeability [4], and optical behaviors [5], [6] are size-dependent. In other words, a nanostructure's property of interest could be finely tuned by manipulating its size and structure. Another quantum mechanical phenomenon of the nanoscale is tunneling, where a particle or wave could tunnel through a classically forbidden potential barrier [7]. Tunneling is a fundamental technique used in the scanning tunneling microscope (STM), resonant-tunneling diode (RTD) and tunneling diode. In addition, nanostructures have far larger surface areas compared to large-scale materials with similar mass, which makes them ideal candidates for catalysts [8], [9] as reactivity could be greatly improved by enlarging contact area with surrounding reacting materials.

For the past three decades, efforts in nanotechnology development have led to a rich amount of nanostructure devices with delicately controlled size, shape and composition. Devices with nanostructures generally fall into two categories: The first category includes materials or devices with dimensionality in the form of nanoparticles, thin wires or films. Quantum dots (QDs),

which are nanoscale semiconductor particles, is a common example of in this category. With three-dimensional (3-D) quantum confinement and tunable optical properties, they have been actively investigated for the development of new generation of light emitting diodes (LEDs) [10] , diode lasers [11], solar cells [12] and transistors [13]. Thin films, consisting of fine layers of materials ranging from nanometers in thickness and micrometers in size, have a broad range of applications in coatings [14], magnetic recording media [15] and batteries. Especially, continuous metal thin films exhibit large transmission due to tunneling effect, which is counter-intuitive when compared with their bulk counterparts. Tunneling effect in thin metal films has attracted much attention and is of value for applications as ultraviolet (UV) transparent conductive coating [16], transparent electrodes for solar cells [17] or photodetectors [18]. Other nanostructures such as nanotubes, nanochains, nanowires have all attracted great interests, and been widely applied in the fields like medicine, bioscience, chemistry, optics and electronics [19]–[22].

The second category comprises bulk devices with nanoscale structure. This category includes either bulk materials or devices with nanoscale structures limited to a thin surface region [23], or those which are assembled of nanoscale building blocks in three dimesons. Common examples in this category are glasses or gels, whose atomic structures vary in space continuously. Photonic crystals (PCs) [24] form another important class. The most original prototype of PCs is a conventional one-dimensional (1-D) thin film stack with alternating materials with different thickness (Fig. 1.1(a)). Such structures are widely used in a variety of applications – from antireflection coatings to highly reflective mirrors. In the 1970s the generalization form of these structures with higher dimensions were proposed by Bykov [25] as a way to inhibit spontaneous

emission. Later in 1987 and 1991, two milestone papers from Yablonovitch [26] and John [27] further proposed to tailor the properties of photons in highly ordered materials with a periodically modulated dielectric constant, and later the term ‘photonic crystal’ is used to refer to such a structure.

The basic idea of PC structures is to mimic the way of how atomic crystals tailor the properties of electrons. Just like the case in electronics, where the periodicity of the atomic lattice leads to the formation of bandgaps and electronic states, certain modes or frequencies will be disallowed when electromagnetic wave propagates through a structure with periodically modulated dielectric constant. Take a 1-D PC as example. When light is incident on an alternating stack of different materials with quarter-wave thickness, each interface reflects some of the light. Certain wavelengths are not allowed to be transmitted due to constructive interference between the reflected fields. As a result, they are 100% reflected. This is the basis of Bragg reflector which is widely used as highly reflective mirrors in laser cavities or thin-film beam splitters. 2-D (Fig. 1.1(b)) and 3-D PCs (Fig. 1.1(c)) can be thought as the generalization form of the 1D case, where a full 2-D or 3-D bandgap appears when the 1-D Bragg reflection condition is satisfied simultaneously for all propagation directions in which the structure is periodic.

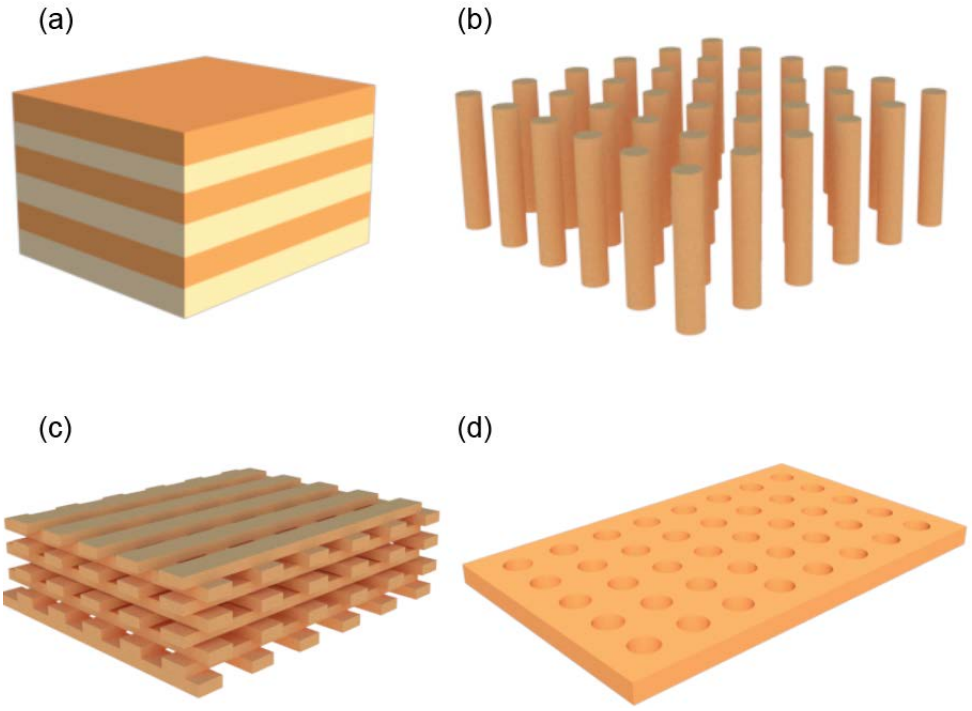

Fig. 1.1 Schematic of a (a) 1-D photonic structure. (b) 2-D photonic structure. (c) 3-D photonic structure. (d) PC slab.

With the presence of a bandgap, one can then confine or route light within the bandgap efficiently by introducing a point, or line defect to the regular lattice. This concept opens up the possibility of producing resonant cavities and waveguides in an integrated form, which attracted much attention soon after the first 2-D bandgap structures were proposed. However, in practice, 2-D PCs which are invariant along the third dimension are impossible to achieve, resulting in out-of-plane loss. 3-D PCs are hard to fabricate due to the complex 3-D connectivity and strict alignment requirements. To enable easier fabrication, PC slab [24] has been proposed as an analogous to 2-D PCs. These are structures consists of a 2-D periodicity induced into a high-index guiding layer so that the in-plane guided modes are completely confined by the slab, as the

one shown in Fig. 1.1(d). Such a structure preserves many desired features of true PCs and could be readily fabricated using a combination of existing nanofabrication techniques such as e-beam lithography, photo-lithography and dry etching.

With the great potential of nanostructures in tailoring photon property, it's clear that it's just beginning to come of age and many possibilities are waiting to be explored. Over the past years, there has been a growing effort in the realization of a number of novel nanostructured devices ranging from laboratory proof-of-concept to commercialized products. In this dissertation, I further explore the applications of nanostructures, including thin films and photonic crystal slabs, in the field of thermal emission, solar cell and spectral sensing.

1.2 Thesis Overview

This dissertation begins with the introduction to nanostructures and the motivation of my research. In chapter 2 I will introduce a spectrally selective thermal emitter based on flat metallic thin film. Infrared thermal emission from metals has important energy applications in thermophotovoltaics, radiative cooling, and lighting. Unfortunately, the emissivity of bulk metals is close to zero because of the screening effect prevents metals' fluctuating currents from emitting to the far field. As a result, bulk metals are often used as reflecting mirrors instead of thermal emitters. On the other hand, nanoscale metal thin film could achieve a near-unity emissivity due to tunneling effect. Simulation results for a 1nm Silver film further proved that emissivity is enhanced over an extremely broad range of spectrum. To achieve spectral selectivity, a Fabry-Perot cavity is used so that the emitting wavelength and bandwidth can be tuned by the cavity length as well as metal film thickness. The performance of the designed

device is then tested in experiment and a near-unity emissivity at selected wavelengths was measured, which agreed well with simulation results.

Chapter 3 introduces the application of Index-Near-Zero (INZ) thin films in solar cell. To increase the efficiency of solar energy conversion, light trapping has been long advocated to increase the optical path length in solar absorbers. It's well known that materials with high refractive index could create longer light-trapping paths and therefore stronger absorption. Alternatively, in this chapter a completely different way of realizing strong light-matter interactions with INZ thin films is introduced. As a result, both the photocurrent and open circuit voltage of the solar cell could be improved. To show INZ thin films could help to increase photocurrent with restricted angle of acceptance, the light trapping limit in such a scheme was derived by applying both statistical ray-optics and rigorous coupled mode theory. The former method is suitable for analyzing the model of traditional cells without nano-patterning while the latter one also applies for nanostructured cells. Both methods proved that the light trapping limit has been greatly improved, indicating a longer optical path length and thus stronger absorption. In addition, detailed balance analysis on a GaAs solar cell showed that the open circuit voltage in the proposed scheme could also be greatly enhanced, as a result of the decreased radiative recombination by INZ films.

In Chapter 4, a method of spectral sensing in nanophotonic structures is proposed theoretically, which is based on compressive sensing. A general mathematical description on the conventional methods for spectral sensing are reviewed first, followed by the details on obtaining spectral information based on compressive sensing. The random bases used in compressive sensing are created by the optical response of a set of different nanophotonic structures. The

proposed method is then tested in simulation for a specific case, where the nanophotonic structure consists of 400 different PC slabs. The performance of this structure is tested by recovering several random signals, including a broadband Lorentz signal with a sharp peak, a spectrum consists of 17 Lorentzian lines as well as 5 Gaussian lines. For all cases the original signals are recovered with high fidelity. The impact of correlation of the response functions and the noise tolerance is also discussed.

Following the theoretical proposal in Chapter 4, Chapter 5 experimentally demonstrates a CMOS-compatible on-chip spectrometer based on a PC slab. Specifically, we implement a two-dimensional array of different PC structures, where the transmission spectrum of individual PC structure is different with each other over a target wavelength range by tuning the pattern shape, size, and lattice constant. This configuration allows each PC structure works as a unique spectral modulator so that the incoming signal is spectrally encoded into transmitted intensity when passing through the structure and collected by a detector underneath. The transmitted intensity distribution over all PC structures is the ‘fingerprint’ to uniquely identify the unknown spectrum using some computational reconstruction methods such as linear regression. It’s shown that the device could achieve 1-2 nm resolution with a total size of 210μm × 210μm. The performance of this device is further tested by measuring some random signals generated by a combination of LEDs and a white light source with a set of filters. Finally, the potential application of this device in hyperspectral sensing is experimentally demonstrated by obtaining the spectral information of the images of some characters on a paper.

Reference

[1] D. W. Prather *et al.*, “Photonic Crystal Structures and Applications: Perspective, Overview, and Development,” *Sel. Top. Quantum Electron. IEEE J. Of*, vol. 12, pp. 1416–1437, Dec. 2006.

[2] R. J. B. Balaguru and B. G. Jeyaprakash, “Melting points, mechanical properties of nanoparticles and Hall Petch relationship for nanostructured materials,” p. 18.

[3] M. Caglar, S. Ilican, Y. Caglar, and F. Yakuphanoglu, “Electrical conductivity and optical properties of ZnO nanostructured thin film,” *Appl. Surf. Sci.*, vol. 255, no. 8, pp. 4491–4496, Feb. 2009.

[4] A. Dimiev *et al.*, “Permittivity of Dielectric Composite Materials Comprising Graphene Nanoribbons. The Effect of Nanostructure,” *ACS Appl. Mater. Interfaces*, vol. 5, no. 15, pp. 7567–7573, Aug. 2013.

[5] F. Flory, L. Escoubas, and G. Berginc, “Optical properties of nanostructured materials: a review,” *J. Nanophotonics*, vol. 5, no. 1, p. 052502, Jan. 2011.

[6] R. J. Gehr and R. W. Boyd, “Optical Properties of Nanostructured Optical Materials,” *Chem. Mater.*, vol. 8, no. 8, pp. 1807–1819, Jan. 1996.

[7] X.-J. Yang *et al.*, “Ultrafast spin tunneling and injection in coupled nanostructures of InGaAs quantum dots and quantum well,” *Appl. Phys. Lett.*, vol. 104, no. 1, p. 012406, Jan. 2014.

[8] F. Zaera, “Nanostructured materials for applications in heterogeneous catalysis,” *Chem. Soc. Rev.*, vol. 42, no. 7, pp. 2746–2762, Mar. 2013.

[9] Z.-A. Qiao, Z. Wu, and S. Dai, “Shape-controlled ceria-based nanostructures for catalysis applications,” *ChemSusChem*, vol. 6, no. 10, pp. 1821–1833, Oct. 2013.

[10] B. Xie, R. Hu, and X. Luo, “Quantum Dots-Converted Light-Emitting Diodes Packaging for Lighting and Display: Status and Perspectives,” *J. Electron. Packag.*, vol. 138, no. 2, pp. 020803-020803–13, Apr. 2016.

[11] I. Samuel, “Colloidal nanocrystals: Electrifying quantum dots for lasers,” *Nat. Mater.*, vol. 17, no. 1, pp. 9–10, Jan. 2018.

[12] A. J. Nozik, “Quantum dot solar cells,” *Phys. E Low-Dimens. Syst. Nanostructures*, vol. 14, no. 1, pp. 115–120, Apr. 2002.

[13] F. Hetsch, N. Zhao, S. V. Kershaw, and A. L. Rogach, “Quantum dot field effect transistors,” *Mater. Today*, vol. 16, no. 9, pp. 312–325, Sep. 2013.

[14] J. R. Arthur *et al.*, “Basic research needs and opportunities in thin films and coatings,” *Mater. Sci. Eng.*, vol. 53, no. 1, pp. 137–148, Apr. 1982.

[15] P. J. Grundy, “Thin film magnetic recording media,” *J. Phys. Appl. Phys.*, vol. 31, no. 21, p. 2975, 1998.

[16] M. Oh, W.-Y. Jin, H. Jun Jeong, M. S. Jeong, J.-W. Kang, and H. Kim, “Silver Nanowire Transparent Conductive Electrodes for High-Efficiency III-Nitride Light-Emitting Diodes,” *Sci. Rep.*, vol. 5, no. 1, Oct. 2015.

[17] K. Patel and P. K. Tyagi, “Multilayer graphene as a transparent conducting electrode in silicon heterojunction solar cells,” *AIP Adv.*, vol. 5, no. 7, p. 077165, Jul. 2015.

[18] W. Luo *et al.*, “Gate Tuning of High-Performance InSe-Based Photodetectors Using Graphene Electrodes,” *Adv. Opt. Mater.*, vol. 3, no. 10, pp. 1418–1423, Oct. 2015.

[19] S. W. Eaton, A. Fu, A. B. Wong, C.-Z. Ning, and P. Yang, “Semiconductor nanowire lasers,” *Nat. Rev. Mater.*, vol. 1, no. 6, Jun. 2016.

[20] B. J. May, A. T. M. G. Sarwar, and R. C. Myers, “Nanowire LEDs grown directly on flexible metal foil,” *Appl. Phys. Lett.*, vol. 108, no. 14, p. 141103, Apr. 2016.

[21] X. Guo, Y. Ying, and L. Tong, “Photonic Nanowires: From Subwavelength Waveguides to Optical Sensors,” *Acc. Chem. Res.*, vol. 47, no. 2, pp. 656–666, Feb. 2014.

[22] W. Tang *et al.*, “Nanochain LiMn2O4 as ultra-fast cathode material for aqueous rechargeable lithium batteries,” *Electrochem. Commun.*, vol. 13, no. 2, pp. 205–208, Feb. 2011.

[23] S. Pandya, A. R. Damodaran, R. Xu, S.-L. Hsu, J. C. Agar, and L. W. Martin, “Strain-induced growth instability and nanoscale surface patterning in perovskite thin films,” *Sci. Rep.*, vol. 6, p. 26075, May 2016.

[24] J. D. Joannopoulos, Ed., *Photonic crystals: molding the flow of light*, 2nd ed. Princeton: Princeton University Press, 2008.

[25] V. P. Bykov, “Spontaneous Emission in a Periodic Structure,” *Sov. J. Exp. Theor. Phys.*, vol. 35, p. 269, 1972.

[26] E. Yablonovitch, “Inhibited Spontaneous Emission in Solid-State Physics and Electronics,” *Phys. Rev. Lett.*, vol. 58, no. 20, p. 4, 1987.

[27] S. John, “Strong localization of photons in certain disordered dielectric superlattices,” *Phys. Rev. Lett.*, vol. 58, no. 23, pp. 2486–2489, Jun. 1987.

CHAPTER TWO

SPECTRALLY SELECTIVE THERMAL EMITTER BASED ON FLAT METALLIC FILMS

2.1 Introduction

A blackbody radiates in a wide spectral range. Such broadband emission is often undesirable in many energy applications that rely on radiative heat as the primary mode of energy exchange. For example, in thermophotovoltaics, an ideal emitter should have a sharp cut-off in the near-infrared spectral range [1]–[3]. In passive radiative cooling [4], the emitter should only radiate in wavelength range between 8 to 13 μm [5]. Driven by these energy applications, there has been a great amount of recent interests in spectrally selective thermal emitters [6]–[13].

There are two approaches to achieve the spectral selectivity. The first relies on the intrinsic dielectric property of materials. For example, SiC is used for thermal emission in the selected spectral range between 10 to 13μm [14] based on its phonon polaritons. Generally, this approach requires minimal amount of nanofabrication because the spectral selectivity is offered by the intrinsic properties of the material. The main drawback is the lack of spectral tunability and potential material incompatibility. The second approach is based on nanostructured materials [15], [16]. This approach offers greater flexibility in tuning the emission spectra because the spectral features are determined by the structure instead of any intrinsic dielectric properties. Metals are often the favorite choice of materials because they can be made to selectively emit at any wavelength from visible to THz. This capability is enabled by the fact that metals' thermal emission mainly comes from free carriers instead of transitions in quantized energy levels.

However, due to the strong screening effect, a flat metal film has very low emissivity. To overcome such issue, recently metamaterial emitters have emerged as a very interesting solution based on the plasmonic resonances of metals. A variety of metallic structures have been demonstrated, including nanoparticles, gratings, and hyperbolic metamaterials [17]–[22], to name a few. Despite its great spectral tunability, using nanostructures to control emission imposes a significant barrier for practical applications because it often requires expensive lithography. It is therefore highly desirable to achieve spectrally selective emitters without nanostructure patterning. In this chapter, a new type of spectral selective emitter based on flat metallic films is reported. Instead of plasmonic resonance, it relies on the tunneling effect in extremely thin films. The tunneling effect enhances the emissivity of metal film over extremely broadband range. A simple Fabry-Perot cavity can be used to accomplish the spectral selectivity. This method allows the large-area low-cost fabrication of spectrally selective thermal emitter, which could be used in a variety of energy applications.

2.2 Tunneling Effect in Extremely Thin Films

Metals have great potential to become efficient thermal emitters because of their high density of free charges. This potential is also reflected by the large value of the imaginary part of the dielectric constant, particularly in the infrared regime. However, the strong screening effect prevents the fluctuating currents inside the metal from radiating to the free space. As a result, flat metal films typically have a low emissivity below 5%. To illustrate such screening effect in simulations, Fig. 2.1(a) shows the emission by an electric-current point source, which can be considered as the building element of a thermal source. The point source emitting at a

wavelength of 10 μm is placed 0.5 nm below the air-silver interface, a distance much shorter than the skin depth (~ 10 nm for silver). The simulation is performed by solving the Maxwell's equations with a finite-element method. The dielectric constant of silver is taken from Ref [23]. One can see that despite being close to the surface, the point source radiates weakly. The bulk Ag material below the point current effectively prevents the far-field emission. Conventional approaches of enhancing the emission in metals exploit the plasmonic resonances in nanostructures, such as metamaterial emitters, which inevitably requires nano-patterning. This chapter explores a completely different mechanism based on the tunneling effect in flat and continuous ultra-thin metal films. To briefly illustrate the idea, Fig. 2.1(b) shows the same current source placed in the center of a 1-nm-thick silver film. Due to the thin thickness, the film does not have enough charges to screen the oscillating current. The emission is drastically enhanced in ultra-thin flat film, which can be directly visualized by comparing Fig. 2.1(a) and Fig. 2.1(b) where the same color map is used. Moreover, unlike the plasmonic resonant enhancement, the tunneling enhancement is a non-resonant effect, meaning that it has extremely broad spectral bandwidth.

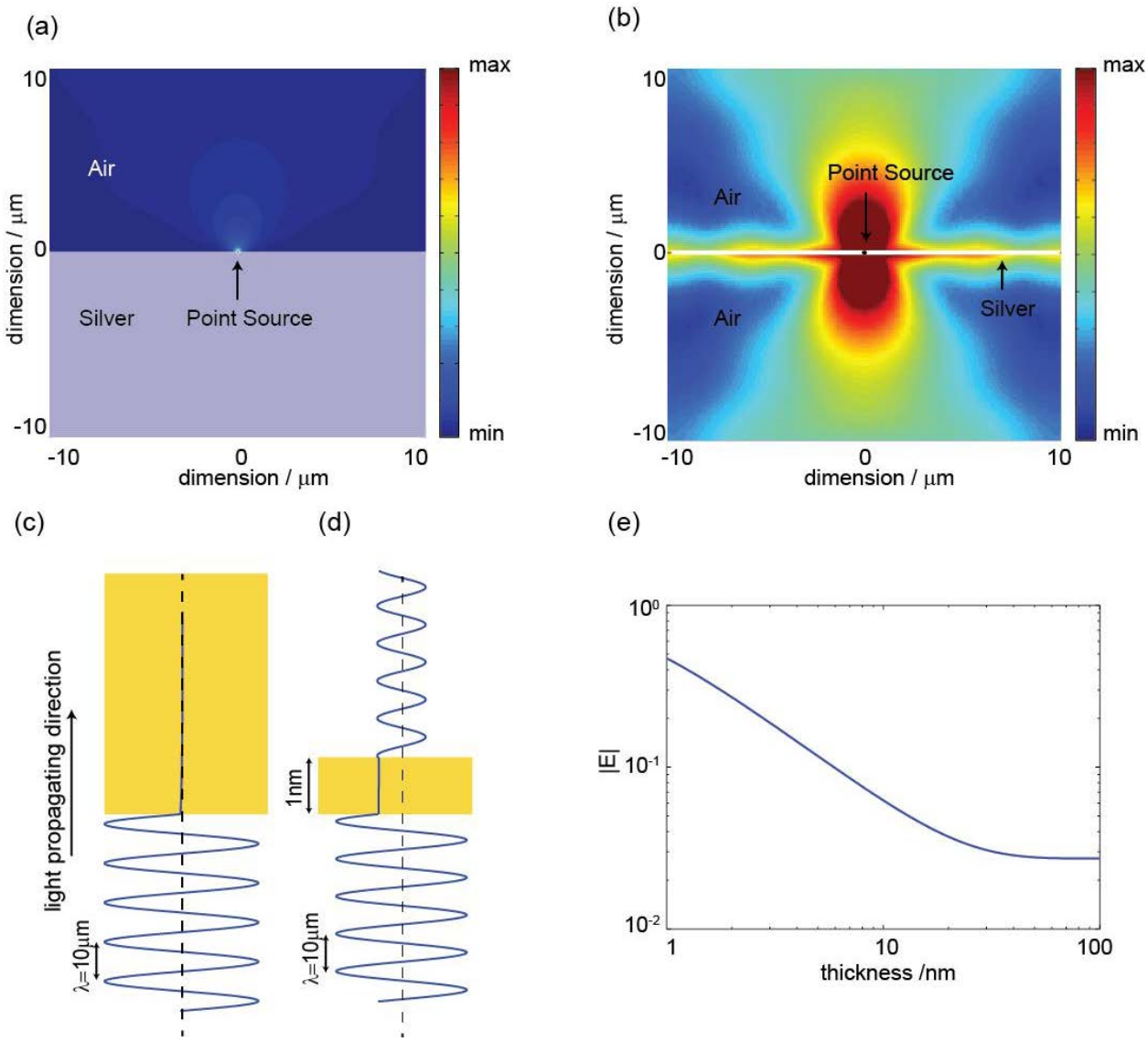

Fig. 2.1 (a) Radiation by an electric-current point source placed 0.5 nm below the interface between air and a semi-infinite silver slab. (b) Radiation by an electric-current point source placed in the center of a 1-nm-thick silver film. (c) – (d) Electric field distributions of light incident normally upon a semi-infinite silver slab (c) and a 1-nm-thick silver film (d). (e) The strength of the electric field at the air-silver interface for silver films of different thickness.

The enhanced emission can also be understood by considering the light absorption of ultra-thin films because the absorption is the reciprocal process of thermal emission. The absorption by a material is linearly proportional to both the imaginary part of the dielectric constant ϵ_{img} and the intensity of electric field $|E|^2$ inside the material. Metals normally have very large ϵ_{imag} in the infrared spectral range. But the electric field inside metals is extremely weak when light shines on a thick metal slab. The electric field can be described as $E\ exp[2\pi(-i\,n-k)x/\lambda]$, where *n* and *k* are the real and imaginary parts of the refractive index of the metal, respectively. Normally, *k* is much larger than *n* for infrared light. The amplitude $|E| \approx 2|E_0|/k$, where E_0 is the amplitude of the incident light. As an example, *n* = 7 and *k* = 73 for silver at the wavelength of 10μm, resulting in an amplitude $|E|$ that is only 2.7% of the incident field $|E_0|$. Fig. 2.1(c) shows the field distribution for a light normally incident upon a thick slab, where the field goes to nearly zero instantaneously in the metal. The resulting absorption and emissivity is extremely weak despite silver's large ϵ_{img} value. On the other hand, for ultra-thin films of a few nanometer thickness, metals are no longer good mirrors, which allow photons to tunnel through. The electric field strength inside the metal is significantly enhanced. In the infrared regime where the wavelength $\lambda \sim 10^3 - 10^4$ nm, the film thickness $d/\lambda \ll 1$ and the amplitude inside the film is comparable to the incident field. Fig. 2.1(d) shows the field distribution for light tunneling through a 1-nm-thick Ag film. The amplitude $|E| = 47\%|E_0|$. Fig. 2.1(e) shows the simulated values of $|E|$ for films of different thicknesses. The tunneling effect is most prominent when the thickness is below 10 nm. As the thickness increases, the tunneling becomes weaker and the amplitude of the field inside silver decreases. When the *d* is thick enough, e.g. thicker than a few tens of nm, it can be treated as a bulk metal and $|E|$ becomes a small constant independent of the

film thickness. Therefore, to obtain an enhanced electric field inside the metal, an ultra-thin film is desired where its absorption and thermal emission can be enhanced.

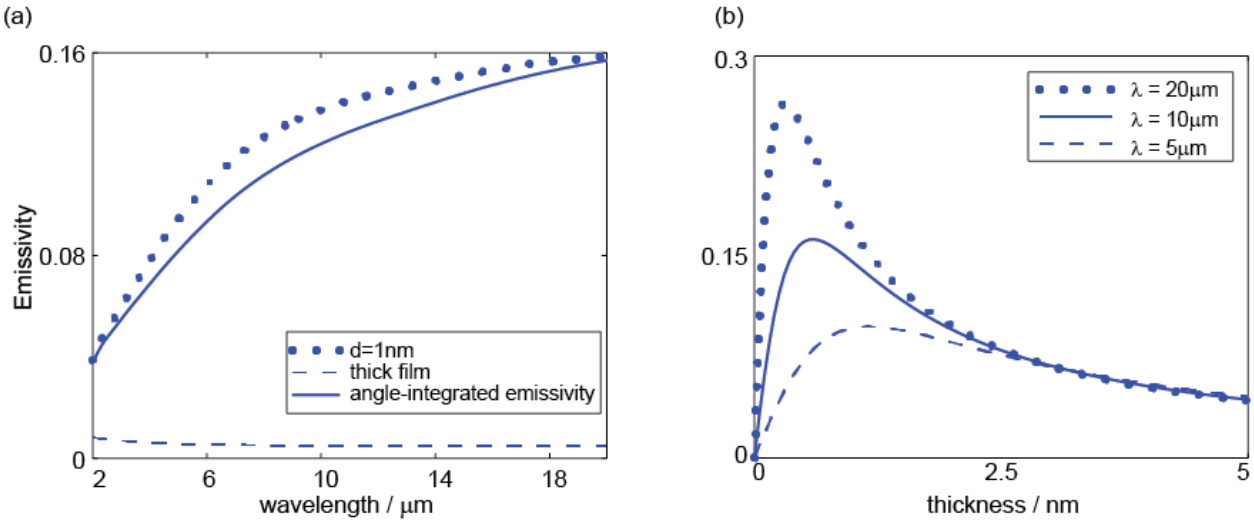

Fig. 2.2 (a) Dotted line: the emissivity of the 1 nm silver film in the direction normal to the surface; dashed line: the emissivity of a bulk silver slab in the normal direction; Solid line: the angle-integrated emissivity of 1 nm silver film. (b) The emissivity as a function of the thickness of the ultra-thin silver film at the wavelengths of 5 μm (dashed), 10 μm (solid) and 20 μm (dotted).

Fig. 2.2(a) compares the spectra of the emissivity of a thick (dashed) and a 1-nm-thick (dotted) silver film in the direction normal to the surface. One can see that the emissivity of the thick film is always less than 1% in the infrared regime. In great contrast, the emissivity of the 1-nm-thick film is up to 16%. More importantly, the emissivity is enhanced over an extremely broad range of spectrum because the tunneling effect does not rely on any optical resonance.

The enhancement due to the tunneling effect is not sensitive to the direction of the thermal

emission. To evaluate the total thermal emission in all angles, I calculated the angle-integrated emissivity defined by

$$e_T = \frac{1}{2}\sum_{s,p}\frac{1}{\pi}\int_0^{\pi/2} d\theta \int_0^{2\pi} d\varphi\, e(\theta,\varphi)\cos(\theta)\sin(\theta) \tag{2.1}$$

where $e(\theta,\varphi)$ is the angle-dependent emissivity. The summation is performed for the two polarization states *s* and *p*. The result for the 1-nm-thick film is shown by the solid line in Fig. 2.2(a). It is almost the same as the emissivity in the normal direction, indicating excellent isotropic emission.

The tunneling effect leads to stronger fields in the metal when reducing the thickness of a film. However, the emissivity will not grow monotonically with a decreasing thickness because the thermal emission also scales with the volume of the materials. For example, for the wavelength of 10 μm, a maximum emissivity of 16.3% is achieved when the film is 0.6 nm thick. Fig. 2.2(b) shows the dependence of emissivity on the thickness of the silver film for the wavelengths of 5 μm (dashed), 10 μm (solid) and 20 μm (dotted). They all reach peak emissivity at certain finite thicknesses.

Another interesting trend can be identified in Fig. 2.2(a) and Fig. 2.2(b): ultra-thin films emit more thermal energy in the longer wavelength range. This trend is somewhat counterintuitive, considering that silver slabs are considered as better mirrors and weaker emitters in the longer wavelength range. Here in ultra-thin films, the amplitude of the field inside metals is on the same scale for different wavelengths, owing to the tunneling effect. However, the imaginary part of the dielectric constant ε_{imag} increases when the wavelength increases, resulting in stronger thermal emission in the long wavelength range.

2.3 Thermal Emitter Design based on Flat Metallic Films

Figs. 2.1 and 2.2 show that the tunneling effect in ultra-thin films can enhance the emissivity over extremely broad spectral range. To achieve spectral selectivity, the simplest approach is to use a Fabry-Perot cavity as shown in Fig. 2.3(a). The cavity consists of three layers: a thick Ag layer as the bottom mirror, a Si layer as the transparent spacer, and an ultra-thin Ag film as the active thermal emitter. The resonance of this cavity further enhances the emissivity at the resonant frequency and suppresses the emissivity at off-resonant frequencies. The wavelength of the emission is primarily determined by the thickness of the spacer.

Fig. 2.3(b) shows the calculated emissivity for different Si spacer thicknesses. The thickness of the silver film is 2 nm. The emissivity is close to unity around the resonant wavelengths. The resonant wavelengths increase as the spacer thickness increases. Higher order cavity modes start to appear with a thicker spacer. As an example, to achieve a selective emitter at the wavelength of 10 μm, a Si spacer of 1.08 μm thick is chosen. For a 2-nm-thick top layer of silver, the peak emissivity reaches 98.2% (Fig. 2.3(c) dashed line). The bandwidth of the selective emitter can also be tuned. The bandwidth is primarily determined by the reflectivity of the top silver film and the length of the cavity. A thinner film leads to a weaker reflectivity and a broader bandwidth. A longer cavity leads to higher quality factor and thus narrower bandwidth. As an example, when reducing the thickness of the silver film from 2 nm to 1 nm, the emission bandwidth is significantly broadened (Fig. 2.3(c) solid line). The cavity also preserves the angular response of ultra-thin film very well. The emissivity for different emission angles at the wavelength of 10 μm is plotted in Fig. 2.3(d), showing high emissivity for broad angular response and for both polarization states.

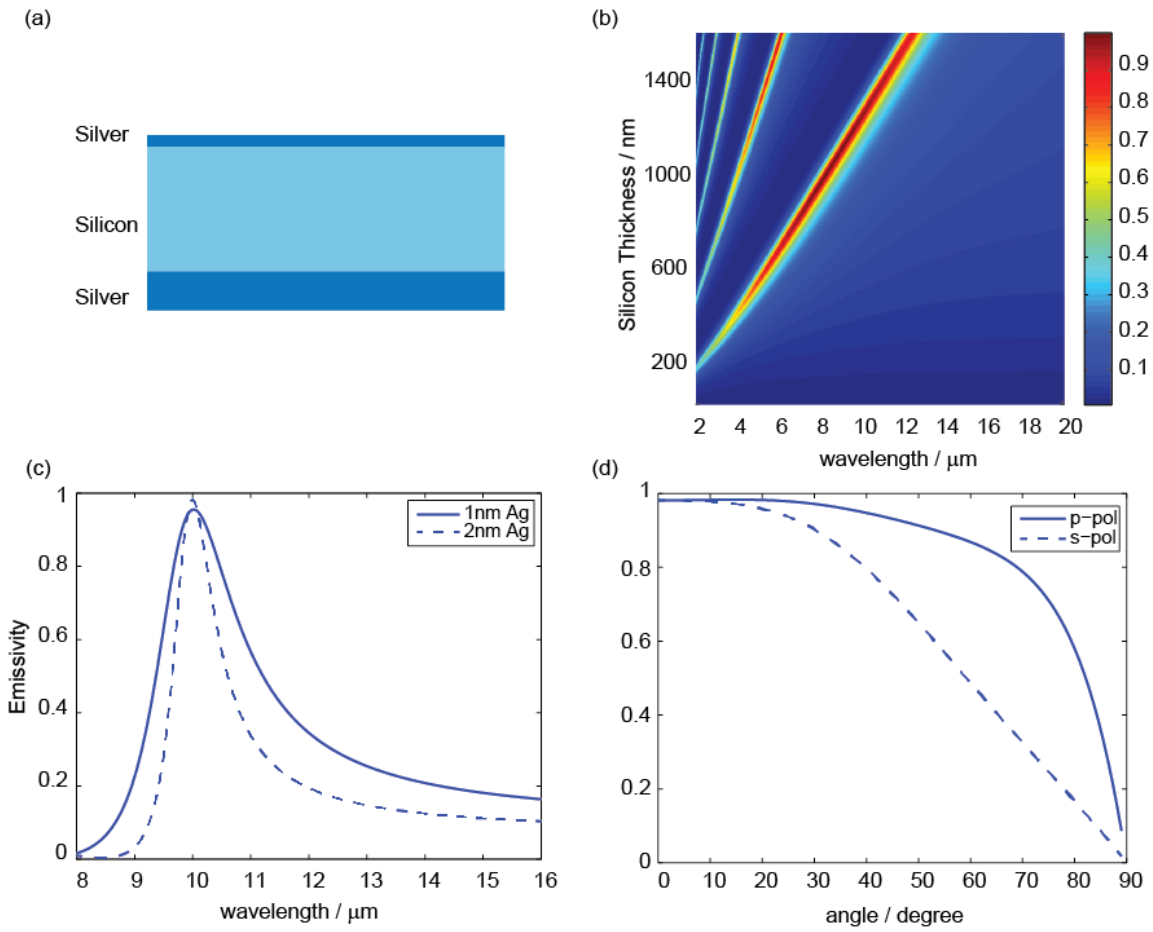

Fig 2.3 (a) The structure of the cavity. (b) The emissivity of the top layer 2 nm Silver in this cavity as a function of both wavelength and Si thickness. (c) The emissivity of the cavity as a function of wavelength. Dashed line: the emissivity of the cavity with 2 nm Ag on top and 1227 nm Si in between; Solid line: the emissivity of the cavity with 1 nm Ag on top and 1077 nm Si in between. (d) The emissivity of the top layer 1 nm silver as a function of incident angle at $\lambda = 10$ μm. Dashed (solid) line is for s (p) polarized light.

2.4 Experimental Demonstration

To experimentally demonstrate spectrally selective emitters based on ultra-thin flat films, a device is fabricated on a Si substrate with root-mean-square (RMS) roughness of < 0.02 nm. Silver films were deposited top of the substrate with a 1-nm-thick Ge film as the wetting layer using electronic beam evaporation. The deposition rate is set to 0.1A/s to control the thickness accurately. The slow deposition rate is important to minimize roughness growth. All films were deposited at room temperature with electron beam thermal evaporation with a typical base pressure of 5×10^{-7} Torr. A 100-nm-thick Ag mirror layer is followed by an 870-nm-thick amorphous silicon layer and finally a 3-nm-thick Ag film. Fig. 2.4(e) shows the photo of a fabricated sample.

This 3-nm-thick Ag film was also deposited on a control glass sample for spectroscopic ellipsometry characterization, which is used to confirm the thickness of the deposited Ag. The thickness and optical constants of the film are fitted in the spectral region from 0.285 to 1 μm. The ellipsometry fit was obtained using Drude model and Tauc-Lorentz oscillator, which is used to describe the interband absorption in the UV spectral region. Fig. 2.4(a) shows the measured ratio $tan(\Psi) = |\frac{r_p}{r_s}|$ between the reflected amplitudes of *s* and *p* polarization lights. Excellent fitted curves are obtained for two different incident angles. The thickness was determined to be 3 nm, agreeing perfectly with the pre-set deposited thickness. The fitted dielectric constants are shown in Fig. 2.4(b).

Sharp rise in curves shown in Fig. 2.4(a) in the short wavelength is a result of sharp transition of dielectric to metallic behavior, a good indicator of high quality silver film. Moreover, the lack of pronounced drop in the spectral feature shown in Fig. 2.4(a) provides evidences that the film

can be considered continuous. There is also no hint of localized surface plasmon absorption feature in the visible region caused by islanding effect of Ag film. The continuity of the thin film is also supported by the atomic force microscopy (AFM) and scanning electron microscope (SEM) measurements shown by Fig. 2.4(c) and Fig. 2.4(d). The SEM image of the top surface indicates the excellent flatness of the surface of a continuous ultra-thin metal film. The RMS roughness measured in the AFM is 0.8 nm, much smaller than the film thickness of 3 nm.

For the characterization of the thermal emission, a heating stage (Linkam, TS1500) installed in a Fourier Transform Infrared spectroscopy (FTIR, Bruker Vertex 70) is used to accurately control the temperature of the sample. The sample is heated to 100 °C in the chamber filled with nitrogen. In order to calculate the emissivity, an area of the emitter is coated with carbon black [24] which has very high emissivity (i.e. ~0.9 of ideal blackbody emissivity) and is used as the normalization reference. As the black carbon is on the emitter directly, it is at the same temperature as the selective emitter. An FTIR microscope (Bruker, Hyperion 1000) is used to selectively characterize different regions of the sample with the area of 400 μm × 400 μm.

Fig. 2.4(f) shows the experimentally measured emissivity for a cavity with a 653 nm thick Si spacer. The emissivity has a peak value close to unity at the wavelength around 9 μm. The emission is suppressed away from the resonant frequency. The Fabry-Perot cavity works very well for the spectral selectivity. The simulation based on fitted dielectric constants is shown by dashed line in Fig. 2.4(f), which agrees very well the experiment. The emissivity also agrees very well with the measured absorption of the sample, which is indicated by the red solid line.

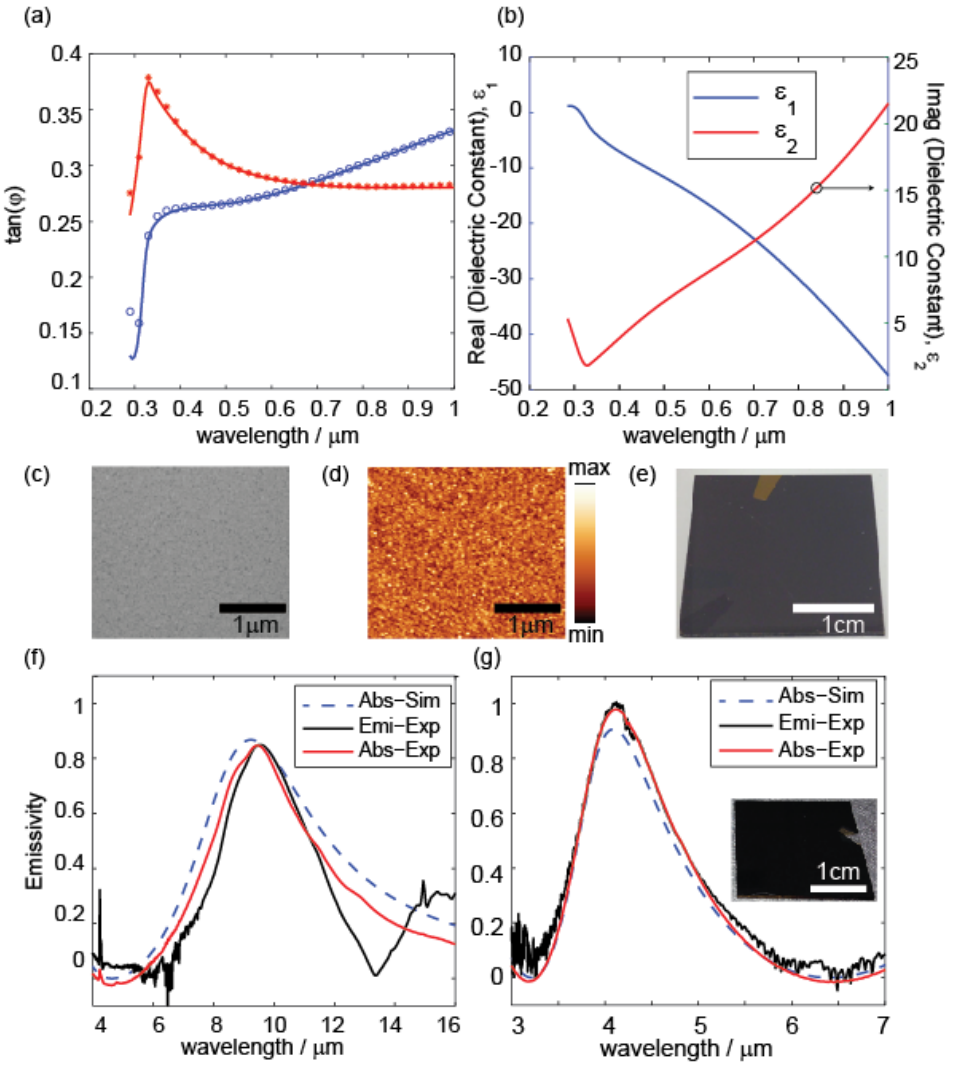

Fig. 2.4 (a) Spectroscopic ellipsometry parameter tan(φ) for a ultra-thin Ag film on a glass substrate. Measured values for incident angles of 60° and 70° are shown by the open-circle and star markers, respectively. The solid lines are the fitted value based on Drude model and Tauc-Lorentz oscillator. (b) Fitted dielectric constants of the silver film. Blue and red curves represent the real and imaginary part of the dielectric constant, respectively. (c) – (e) SEM (c) image, AFM (d) image, and photography(e) of the sample. (f) Measured emissivity (black line) and absorption (red line) for the spectrally selective emitter. Dashed line is the simulated emissivity. (g) Tuning

the emission frequency by varying the length of the cavity. The measured emissivity (black solid), measured absorption (red solid) and the simulated emissivity for a cavity with a Si spacer that is 874 nm thick. The top layer is 3 nm thick silver. The inset shows the photograph of the fabricated sample.

Thus the wavelength of thermal emission is easily tuned by controlling the thickness of Si slab. For this purpose, another cavity with an 874-nm-thick Si spacer and a 3-nm-thick silver film is fabricated. The same characterization is performed. The results are shown in Fig. 2.4(g). The wavelength of the second order Fabry-Perot mode is around 4 μm. Indeed, enhanced thermal emission at this wavelength with an emissivity close to unity is observed. The measured absorption and simulated emissivity all agree very well with the measured emissivity.

2.5 Conclusion

Large-area spectrally selective thermal emitters are a critical component in energy conversion applications. The existing methods based on metamaterial metallic structures are not suitable for low-cost large-area applications because of the expensive lithography processes. This chapter proposed and experimentally demonstrated a new emission mechanism based on the tunneling effect, which enables a flat metallic film to efficiently emit thermal energy at selected wavelengths. Without involving any nano-patterning, the tunneling-enabled emission offers an extremely simple and low-cost method to obtain large area spectrally-selective emitters.

Reference

[1] A. Lenert *et al.*, "A nanophotonic solar thermophotovoltaic device," *Nat. Nanotechnol.*, vol. 9, no. 2, pp. 126–130, Feb. 2014.

[2] E. Rephaeli and S. Fan, "Absorber and emitter for solar thermo-photovoltaic systems to achieve efficiency exceeding the Shockley-Queisser limit," *Opt. Express*, vol. 17, no. 17, p. 15145, Aug. 2009.

[3] A. Narayanaswamy and G. Chen, "Surface modes for near field thermophotovoltaics," *Appl. Phys. Lett.*, vol. 82, no. 20, pp. 3544–3546, May 2003.

[4] A. P. Raman, M. A. Anoma, L. Zhu, E. Rephaeli, and S. Fan, "Passive radiative cooling below ambient air temperature under direct sunlight," *Nature*, vol. 515, no. 7528, pp. 540–544, Nov. 2014.

[5] E. Rephaeli, A. Raman, and S. Fan, "Ultrabroadband Photonic Structures To Achieve High-Performance Daytime Radiative Cooling," *Nano Lett.*, vol. 13, no. 4, pp. 1457–1461, Apr. 2013.

[6] M. U. Pralle *et al.*, "Photonic crystal enhanced narrow-band infrared emitters," *Appl. Phys. Lett.*, vol. 81, no. 25, pp. 4685–4687, Dec. 2002.

[7] S. Y. Lin, J. Moreno, and J. G. Fleming, "Three-dimensional photonic-crystal emitter for thermal photovoltaic power generation," *Appl. Phys. Lett.*, vol. 83, no. 2, pp. 380–382, Jul. 2003.

[8] M. Laroche *et al.*, "Highly directional radiation generated by a tungsten thermal source," *Opt. Lett.*, vol. 30, no. 19, pp. 2623–2625, Oct. 2005.

[9] M. Laroche, R. Carminati, and J.-J. Greffet, “Coherent Thermal Antenna Using a Photonic Crystal Slab,” *Phys. Rev. Lett.*, vol. 96, no. 12, Mar. 2006.

[10] P. Nagpal, S. E. Han, A. Stein, and D. J. Norris, “Efficient Low-Temperature Thermophotovoltaic Emitters from Metallic Photonic Crystals,” *Nano Lett.*, vol. 8, no. 10, pp. 3238–3243, Oct. 2008.

[11] M. D. Zoysa, T. Asano, K. Mochizuki, A. Oskooi, T. Inoue, and S. Noda, “Conversion of broadband to narrowband thermal emission through energy recycling,” *Nat. Photonics*, vol. 6, no. 8, pp. 535–539, Aug. 2012.

[12] B. J. Lee, C. J. Fu, and Z. M. Zhang, “Coherent thermal emission from one-dimensional photonic crystals,” *Appl. Phys. Lett.*, vol. 87, no. 7, p. 071904, Aug. 2005.

[13] J. A. Schuller, T. Taubner, and M. L. Brongersma, “Optical antenna thermal emitters,” *Nat. Photonics*, vol. 3, no. 11, pp. 658–661, Nov. 2009.

[14] N. I. Landy, S. Sajuyigbe, J. J. Mock, D. R. Smith, and W. J. Padilla, “Perfect Metamaterial Absorber,” *Phys. Rev. Lett.*, vol. 100, no. 20, May 2008.

[15] N. Liu, M. Mesch, T. Weiss, M. Hentschel, and H. Giessen, “Infrared Perfect Absorber and Its Application As Plasmonic Sensor,” *Nano Lett.*, vol. 10, no. 7, pp. 2342–2348, Jul. 2010.

[16] M.-W. Tsai, T.-H. Chuang, C.-Y. Meng, Y.-T. Chang, and S.-C. Lee, “High performance midinfrared narrow-band plasmonic thermal emitter,” *Appl. Phys. Lett.*, vol. 89, no. 17, p. 173116, Oct. 2006.

[17] K. Aydin, V. E. Ferry, R. M. Briggs, and H. A. Atwater, “Broadband polarization-independent resonant light absorption using ultrathin plasmonic super absorbers,” *Nat. Commun.*, vol. 2, p. 517, Nov. 2011.

[18] C. Wu *et al.*, "Metamaterial-based integrated plasmonic absorber/emitter for solar thermo-photovoltaic systems," *J. Opt.*, vol. 14, no. 2, p. 024005, Feb. 2012.

[19] Y. Cui *et al.*, "Ultrabroadband Light Absorption by a Sawtooth Anisotropic Metamaterial Slab," *Nano Lett.*, vol. 12, no. 3, pp. 1443–1447, Mar. 2012.

[20] H.-J. Hagemann, W. Gudat, and C. Kunz, "Optical constants from the far infrared to the x-ray region: Mg, Al, Cu, Ag, Au, Bi, C, and Al_2O_3," *JOSA*, vol. 65, no. 6, pp. 742–744, Jun. 1975.

[21] H. Hu, D. Ji, X. Zeng, K. Liu, and Q. Gan, "Rainbow trapping in hyperbolic metamaterial waveguide," *Sci. Rep.*, vol. 3, p. 1249, 2013.

[22] J. Hao, L. Zhou, and M. Qiu, "Nearly total absorption of light and heat generation by plasmonic metamaterials," *Phys. Rev. B*, vol. 83, no. 16, p. 165107, Apr. 2011.

[23] G. E. Jellison and F. A. Modine, "Parameterization of the optical functions of amorphous materials in the interband region," *Appl. Phys. Lett.*, vol. 69, no. 3, pp. 371–373, Jul. 1996.

[24] Z. Yu, N. P. Sergeant, T. Skauli, G. Zhang, H. Wang, and S. Fan, "Enhancing far-field thermal emission with thermal extraction," *Nat. Commun.*, vol. 4, p. 1730, Apr. 2013.

CHAPTER THREE

PHOTON MANAGEMENT WITH INDEX-NEAR-ZERO THIN FILM

3.1 Introduction

The goal of photon management is to increase the efficiency of solar energy conversion through enhanced light-matter interactions. High-index materials have been long advocated for this purpose [1] because their high optical density of states (DOS) creates strong light-matter interactions [2]–[4]. Specifically, the technique of light trapping has been developed to exploit high-index materials to increase the optical path length in solar absorbers. Fig. 3.1(a) shows the classical setup of light trapping. An absorber with a refractive index *n* is placed on the top of a Lambertian mirror. When incident sunlight passes through the absorber and reaches the mirror, the reflection direction is randomized. Light rays with large reflection angles propagate for longer distances. They can even go through multiple reflections to accumulate optical paths that are much longer than the absorber thickness *d*. A longer path indicates stronger light absorption, which is desirable for solar cells. Yablonovitch developed a statistical ray optics theory and showed that the average path length l_e is subject to the light-trapping limit [2] *F*

$$F = \frac{l_e}{d} \leq 4n^2 \tag{3.1}$$

It shows that a higher index material could create longer light-trapping paths and therefore stronger light absorption. High-index materials such as Si and GaAs, afford a much better light-trapping performance than the low-index ones, such as polymers. The understanding of this light-trapping limit has significantly contributed to the development of high-efficiency solar cells

in the past decades. It has been generally believed that low-index materials are undesirable for photon management.

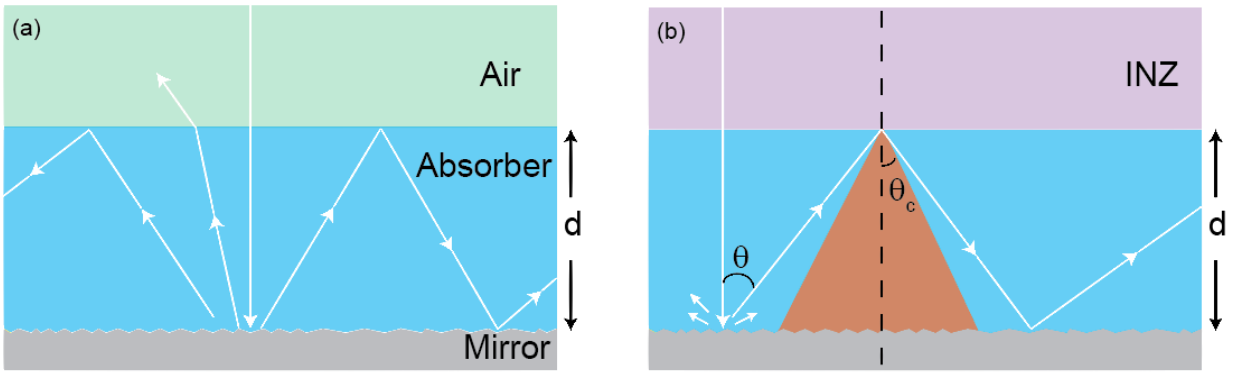

Fig. 3.1 (a) Schematic of conventional light-trapping. The solar absorber (blue color in the middle) is placed on top of a perfect Lambertian mirror (gray at the bottom). (b) Schematic of ray-tracing theory. The INZ material is represented by the purple color on the top. Light rays are represented by white arrows.

In a stark contrast to this conventional wisdom, this chapter shows that an emerging optical material with ultra-low DOS could provide a completely different way of realizing strong light-matter interactions. These materials, also named index-near-zero (INZ) materials [5]–[12] have refractive indices smaller than vacuum. Intriguing effects have been found in INZ materials such as cloaking [13], [14],bending with small curvature [15]–[17], and super scattering [18]. This chapter shows that INZ materials also exhibit exciting potentials to realize light-trapping performance far better than the conventional limit. Moreover, INZ materials can also improve the photovoltaic voltage owing to the suppression of radiative emission. Such voltage enhancement cannot be realized by conventional high-index materials. It allows single-junction

solar cells to achieve efficiencies greater than the Shockley-Queisser limit [19] under one sun.

3.2 Light Absorption Enhancement with INZ Thin Film

3.2.1 Light Trapping Limit Derived by Ray-Tracing Method

A ray-tracing theory is applied first to show the fundamental limit of light trapping in INZ materials. Fig. 3.1(b) shows a solar absorber with a cladding layer of INZ material. The absorber is made from conventional semiconductors. It is placed on a perfect Lambertian mirror. Perfect anti-reflection is used at all interfaces. The INZ material increases the light-trapping limit to:

$$F \leq \frac{4n^2}{{n_{inz}}^2} \tag{3.2}$$

where n_{inz} is the index of the INZ material. With an index $n_{inz} \ll 1$, this limit can go far beyond the Yablonovitch limit $4n^2$. For instance when $n_{inz} = 0.1$, the limit is $400n^2$. It is two orders of magnitude higher than the conventional Yablonovitch limit $4n^2$, indicating extraordinarily long optical paths and strong sunlight absorption in the absorber.

To prove the above limit, the path of a normally incident light ray is traced. It first travels a distance of d to reach the bottom mirror as shown in Fig. 3.1(b). Then it is reflected by the diffusive mirror and propagates in a random direction θ. The path length of the reflected light is $d/\cos\theta$ when it reaches the INZ-absorber interface. Considering the randomness of the reflection angle, the average light path can be calculated as

$$\frac{\iint \frac{d}{cos\theta} cos\theta d\Omega}{\iint cos\theta d\Omega} = 2\mathrm{d} \tag{3.3}$$

Here the probability distribution of the reflection angle is $\cos\theta/(\iint \cos\theta \mathrm{d}\Omega)$ and the $\cos\theta$ factor accounts for the power distribution reflected by a Lambertian surface. Not all light that reaches

the INZ-absorber interface can escape to the outside. Totally internal reflection defines an escape cone with an apex angle of $\theta_c = sin^{-1}(n_{inz}/n)$ as shown by the brown cone in Fig. 3.1(b). The reflected light can escape only when $\theta < \theta_c$. The probability of such an event is n_{inz}^2/n^2. For $\theta \geq \theta_c$, light is trapped and propagates toward the Lambertian mirror which randomizes its direction again. By tracing the path in an infinite series of reflections, the average light path length is obtained

$$l_e = d + 2d + 4d\left(1 - \frac{{n_{inz}}^2}{n^2}\right) + 4d\left(1 - \frac{{n_{inz}}^2}{n^2}\right)^2 + \cdots = (\frac{4n^2}{{n_{inz}}^2} - 1)d \qquad (3.4)$$

the absorption loss has been neglected, following the standard assumption used in deriving the light-trapping limit. Above equation directly leads to the limit in Eq. (3.1). This ray-tracing theory shows that conventional high-index absorbers improve conventional light trapping because a high-index *n* reduces the size of the escape cone $sin^{-1}(n_{inz}/n)$. Here, INZ materials introduce an alternative way to reduce the escape cone by using $n_{inz} < 1$.

3.2.2 Light Trapping Limit Derived by Rigorous Wave Theory

The ray-tracing theory is intuitive. However, many INZ materials and thin-film absorbers heavily rely on nanostructures. The optical interferences and diffraction make it difficult to treat light as rays. In addition, the light-trapping limit in nanostructures also differs from the conventional Yablonovitch limit [3]. Next, rigorous wave theory is used to show the limit of light trapping when INZ materials are applied to nanostructured materials.

3.2.2.1 Light Trapping Limit in 3-D space

Without loss of generality, a model of a periodic nanostructured absorber with a period *L* is

considered. Non-periodic structures can be understood by taking the limit of $L \to \infty$. The wave effects make it impossible to trace the light path. To overcome this issue, the absorption enhancement factor $\mathbb{F} = A/\alpha d$ is calculated first, where A and d are the absorptance and the average thickness of the absorber, respectively. α is the intrinsic absorption coefficient of the material. The light-trapping limit, i.e., the maximum enhancement of light path length F, can then be obtained by [3]

$$F = \lim_{\alpha d \to 0} \mathbb{F}. \tag{3.5}$$

Because in the weak absorption limit when $\alpha d \to 0$, light absorption A is linearly proportional to the light path length l. Therefore, the absorption enhancement factor $\mathbb{F}$ provides a direct measure of the light-trapping limit F.

There is another wonderful consequence as $\alpha d \to 0$: all light absorption is contributed by optical resonance. Non-resonant absorption can be safely neglected. As a result, light absorption can be conveniently evaluated by the summation of the absorption of all resonances. For a single resonance, the maximum broadband absorption is $\sigma_{max} = \int_0^\infty A(\omega) d\omega = 2\pi\gamma/N$, where N is the number of diffraction beams created by the periodic nanostructure. γ is the intrinsic absorption rate of the resonance, defined by the ratio between the amount of light energy absorbed per unit of time and the total energy stored in the resonance. As a good approximation, $\gamma = \alpha c/n$ with c being the speed of light in vacuum. The light absorption is simply the summation of the absorption by all resonances $A = M\sigma_{max}/\Delta\omega$, where M is the total number of resonances in the spectral range between ω and $\omega + \Delta\omega$. The upper limit of light absorption enhancement can be calculated as [3]

$$\mathbb{F} = \frac{A}{\alpha d} = \frac{2\pi\gamma}{\alpha d \Delta\omega} \times \frac{M}{N} \tag{3.6}$$

Eq. (3.6) applies to both bulk and nanostructured absorbers. For bulk absorbers, one can use the standard bulk DOS to calculate the number of resonances $M_{bulk} = \frac{8\pi n^2 \omega^3}{c^3}\left(\frac{L}{2\pi}\right)^2 (\frac{d}{2\pi})\Delta\omega$, which would reproduce the conventional $4n^2$ limit. In the nanostructures, previous research efforts have mainly focused on designing the DOS of nanostructured absorbers such that it exceeds M_{bulk} [3], [4]. Here, INZ materials realize enhancement through a completely different mechanism. They do not enhance the DOS and *M*. Instead, their ultra-low index significantly reduces the number of diffraction beams *N*.

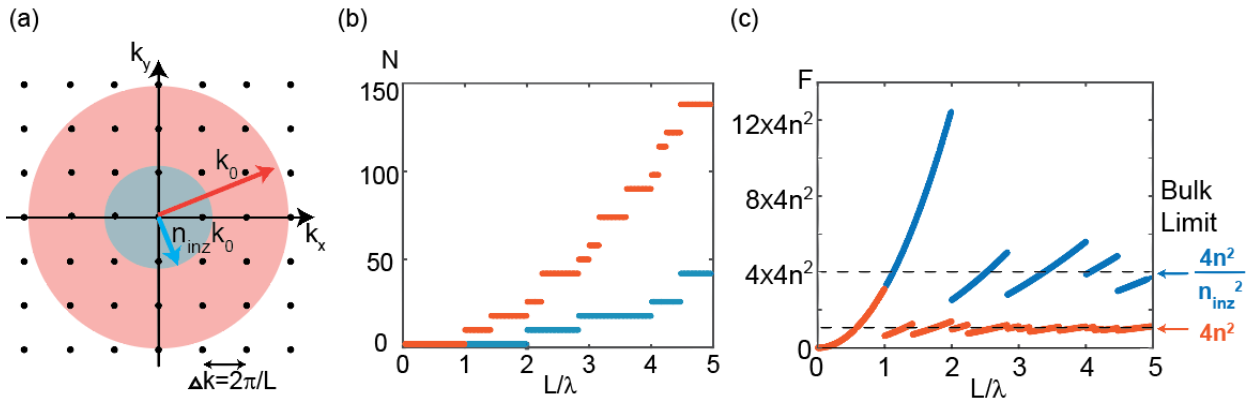

Fig. 3.2 (a) Schematic of the k-space for deriving the nanophotonic light-trapping limit. Dots represent all waves that satisfy the boundary condition. The index of the material above the absorber defines a circle where propagating wave can escape. The circle for vacuum (red) is larger than that for an INZ material (blue). (b) The number of diffraction beams *N* for the cases with vacuum (red) and an INZ material (blue) above the absorber. n_{inz} = 0.5. (c) Nanophotonic light-trapping limit with vacuum (red) and an INZ material (blue).

The impact of *N* on light trapping based on the case without INZ materials [20] is reviewed

first. The diffraction beams created by a periodic nanostructure can be described by a set of plane waves shown by the dots in the *k*-space in Fig. 3.2(a). They are spaced by $\Delta k = 2\pi/L$. *N* is the number of dots inside the propagating-wave circle of a radius k_0 (red area in Fig. 3.2(a)). Outside the circle are the evanescent waves. The light-trapping limit strongly depends on the period *L* because *L* dictates the density of dots in the *k*-space. Such wave effect is absent in the ray-tracing theory. As the period *L* increases, *N* increases in steps (red lines in Fig. 3.2(b)) while the number of resonance per unit cell *M* also increases. The resulting light trapping limit can be calculated from Eq. (3.6) and is shown by the red lines in Fig. 3.2(c). When the period is around wavelength $L/\lambda \sim 1$, the light-trapping limit deviates significantly from the bulk $4n^2$ limit. When $L/\lambda \gg 1$, the limit approaches the ray-tracing limit $4n^2$, which is expected because the wave effects are less pronounced in large-period structures.

Next, how INZ materials affect the above wave-based analysis is evaluated. With an INZ material above the nanostructured absorber, the radius of the propagating-wave circle is reduced by a factor of n_{inz} (blue area in Fig. 3.2(a)). Consequently, there are fewer diffraction beams (blue lines in Fig. 3.2(b)) while the number of resonances *M* remains the same because the absorber is the same. As a result, the light-trapping limit is higher than that without the INZ material (blue lines in Fig. 3.2(c)). Again, as the period increases, the limit converges to $4n^2/n_{inz}^2$, which agrees excellently with the ray-tracing theory.

To validate the theory described above, light absorption is simulated by numerically solving the full-wave Maxwell's equations. While the enhancement is intrinsically broadband, my simulation focuses on a normalized spectral range between λ_0 to $1.15\lambda_0$ to reduce the required computational resources. The structure of the simulated solar cell is shown in Fig. 3.3(a). It

consists of an absorber with a thickness of $d = 5\lambda_0$ with the surface structure of the unit cell shown in Fig. 3.3(b). The period is $L = 3\lambda_0$. It is weakly absorptive with $\alpha d = 0.0006$. The absorber is placed on top of a mirror and below an INZ thin film with $1.7\lambda_0$ thickness. The refractive indices for the absorber and the INZ material are n= 3.5 and n_{inz}= 0.33, respectively. Anti-reflection layers are used at interfaces. We use the S^4 [21] method to calculate the light absorption for normally incident light. Comparing to the single path absorption αd, the polarization-averaged enhancement factor $\mathbb{F}$ is shown in Fig. 3.3(c). The spectrum consists of many sharp peaks caused by numerous resonances in the structure. The average absorption enhancement is $\overline{\mathbb{F}} = 823$, which agrees with the theoretical upper limit 1226 reasonably well. In comparison, the enhancement factor of the Yablonovitch limit is only 49. The INZ material increases the light-trapping limit by more than one order of magnitude and it is higher than any light-trapping limit reported so far.

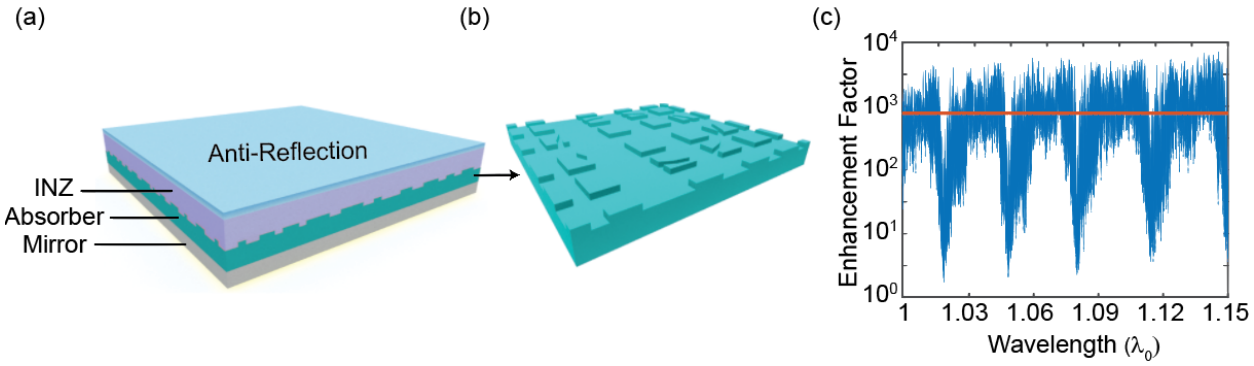

Fig. 3.3 (a) The periodic nanostructure used for simulation. (b) The surface structure of the absorber shown in (a). (c) The spectrum of the light absorption enhancement factor for the structure shown in (a).

3.2.2.2 Light Trapping Limit in 2-D space

In addition to the light trapping limit derived for 3-D space, here I will use rigorous wave theory to derive the light trapping limit in 2-D space.

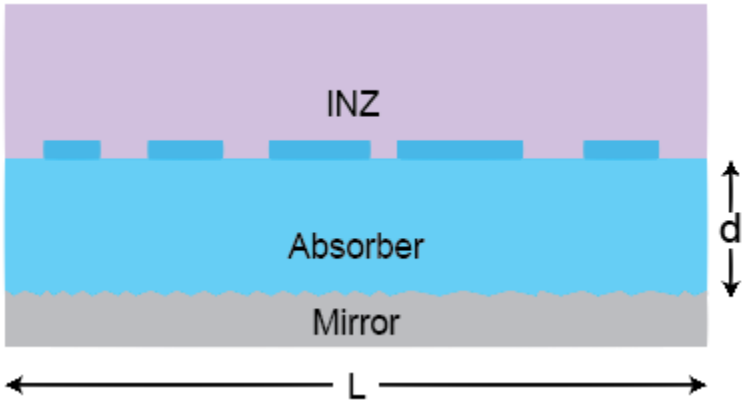

Fig. 3.4 Structure for deriving the light-trapping limit in 2-D space. The solar absorber (blue color in the middle) is placed on top of a perfect Lambertian mirror (gray at the bottom). The INZ material is represented by the purple color on top.

As shown in Fig. 3.4, the 2D solar cell consists of an absorber with refractive index n and an averaged thickness of d. The absorber is placed below an INZ material with refractive index n_{inz} and on top of a perfect Lambertian mirror. Based on Eq. (3.6), for a 2-D case,

$$\gamma = \frac{\alpha c}{n} \tag{3.7}$$

with c being the speed of light in vacuum. M can be calculated using the standard DOS of bulk material

$$M = \frac{2n^2\pi\omega}{c^2}\left(\frac{L}{2\pi}\right)\left(\frac{d}{2\pi}\right)\Delta\omega \tag{3.8}$$

which remains the same with or without INZ. And to calculate the number of diffracted beams *N*, first I need to claim two conditions that the diffracted beams should satisfy. First, as a result of the periodicity of the 2D structure, the parallel components of the wave vectors of all the diffracted beams should have the form

$$k_{//} = m\frac{2\pi}{L}$$

where m is an integer. Second, in order to satisfy boundary condition at the INZ-absorber interface, $k_{//}$ should be always less than $n_{inz}k_0$. Based on these two constrains, the number of diffracted beams *N* can be calculated as

$$N = \frac{2n_{inz}k_0}{2\pi/L} = \frac{2\pi}{\lambda}n_{inz} \tag{3.9}$$

when $L >> \lambda$. Combining Eqs. (3.6)-(3.9), the upper limit of enhancement factor for INZ materials in 2D space can be calculated as

$$F_{2D} = \frac{\pi n}{n_{inz}} \tag{3.10}$$

3.3 Open-Circuit Voltage Improvement by INZ Thin Film

The light-trapping limit discussed above only concerns about the light absorption, which mainly helps to improve the photocurrent of solar cells. In addition, INZ materials can also improve another important property of solar cells: the open-circuit voltage. Specifically, the small phase space in INZ materials suppresses the radiative emission. This suppression can be intuitively understood by considering a perfect blackbody placed inside an INZ material. The density of thermal radiation energy is $n_{inz}^2\sigma T^4$ with σ and T being the Stefan-Boltzmann

constant and the temperature, respectively. This emitted power is n_{inz}^2 times lower than the standard Stefan-Boltzmann law in vacuum. The same suppression also occurs in semiconductors, where INZ materials decrease the radiative recombination rate of photo-generated carriers. This suppression greatly benefits direct-bandgap solar cells [22] by improving the open-circuit voltage V_{oc}. The increased V_{oc} results in an efficiency above the standard Shockley-Queisser limit [19], even in a single-junction cell operating under one sun.

For a specific example, GaAs cells are studied as shown in the inset in Fig. 3.5(a). For simplicity, all dimensions of the solar cells are taken to be much larger than both the optical wavelengths as well as the absorption length of GaAs. All non-idealities such as non-radiative recombination, and interfacial reflections are also excluded. These assumptions are standard in deriving the fundamental limit of the energy efficiency in direct bandgap solar cells and they are well justified in realistic high-quality GaAs cells [22]. Following the detailed balance analysis, the carrier generation rate F_g created by the sun must equal the recombination rate [19]

$$F_g = I + \exp\left(\frac{eV_{oc}}{k_B T}\right) F_o \tag{3.11}$$

where e, and k_B are the elementary charge and the Boltzmann constant, respectively. I is the current. The generation rate F_g is

$$F_g = \int_{E_g/\hbar}^{\infty} S(\omega) d\omega \tag{3.12}$$

where $S(\omega)$ is the photon flux density from the sun and E_g is the bandgap energy of the semiconductor. On the right hand side of Eq. (3.11), F_o is the flux density of photons emitted by the absorber as a result of thermal fluctuation at the thermal equilibrium [23]–[25]

$$F_o = 2\pi \int_0^{\theta_c} d\theta \int_{E_g/\hbar}^{\infty} d\omega \cos\theta \sin\theta \Theta(T,\omega) \tag{3.13}$$

where $\Theta(T,\omega) = \frac{n^2\omega^2}{4c^2\pi^3}\left[\exp\left(\frac{\hbar\omega}{kT_c} - 1\right)\right]^{-1}$ is the thermal photon flux density in the absorber. It is important to note that the integration starts from the normal direction $\theta = 0$ to the critical angle $\theta_c = \sin^{-1}(n_{inz}/n)$. For photons' directions $\theta > \theta_c$, there will be complete photon recycling and it does not contribute to the radiative recombination.

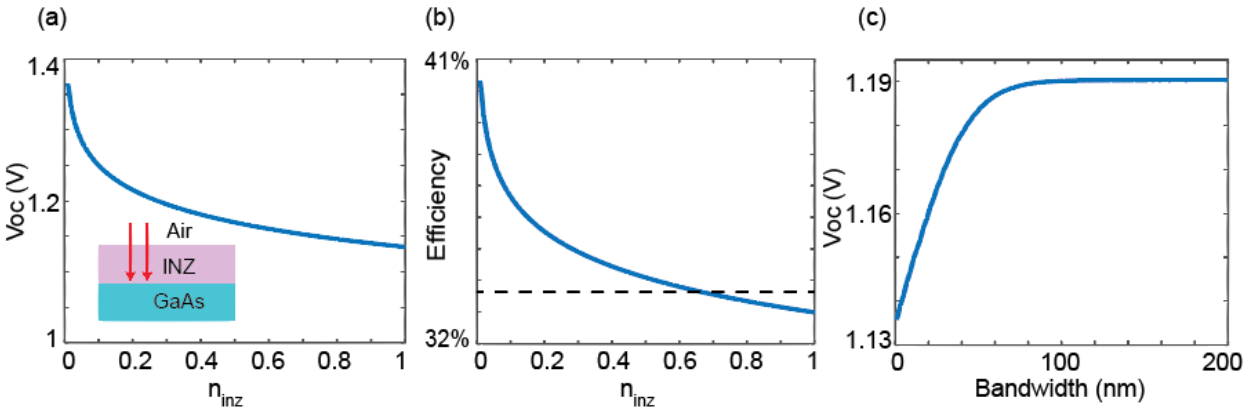

Fig. 3.5 (a) Calculated V_{oc} as a function of n_{inz} for ideal GaAs solar cells with a cladding of INZ material. GaAs absorber is thick enough to absorb all incident light and is placed on a mirror. (b) Maximum efficiency as a function of the index of the cladding INZ material. The Shockley-Quiesser limit of energy conversion efficiency is indicated by the dashed line (c) V_{oc} as a function of the bandwidth of the INZ material. Inside the spectral bandwidth $n_{inz} = 0.33$ while outside $n_{inz} = 1$.

Combining Eqs. (3.11) – (3.13), we can solve for the current-voltage relationship. Using GaAs at the open circuit condition $I = 0$, the open circuit voltage V_{oc} is calculated as a function of

n_{inz} (Fig. 3.5(a)). When $n_{inz} = 1$, the result is identical to conventional detailed balance modeling, which produces the result from standard Shockley-Queisser analysis at 1.14 V. As n_{inz} decreases, the open circuit voltage increases. For example, when $n_{inz} = 0.1$, V_{oc} increases by more than 100 mV (Fig. 3.5(a)). As a result of the increasedV_{oc}, the efficiency of energy conversion also increases. As shown by Fig. 3.5(b), it reaches over 40% for small indices. The use of INZ materials increases the energy conversion efficiency well above the Shockley-Quiesser limit [19] of 33.7% for single-junction solar cells under one sun, which is indicated by the dashed line in Fig. 3.5(b).

3.4 Discussion

Finally, I comment on the optical loss and spectral bandwidth of INZ materials. Lossless INZ materials were recently demonstrated [17], [26] in structured dielectric materials. They do not use metals and thus are free from any light absorption. Even for those INZ materials that do use metals, rapid progress has been made toward low loss INZ materials [27], [28]. While broadband INZ materials [29], [30] are emerging, it is also important to emphasize that one does not need broadband INZ material to realize all the enhancement effects shown above. Because most radiative recombination occurs in the close vicinity of the bandgap frequency, a narrow band INZ would be equally effective in improving the open circuit voltage. As shown in Fig. 3.5(c), an index $n_{inz} = 0.33$ with a limited bandwidth in the frequency range right above $E_g/\hbar$ is used. Even a 50 nm wavelength bandwidth produces an impressive enhancement of V_{oc}.

3.5 Conclusion

This chapter shows a new mechanism for realizing strong light-matter interactions. Unlike conventional approaches that use high optical DOS, this photon management method exploits the ultra-low DOS in INZ materials to confine light in the absorbers. It is known that restricting the angular response of a solar cell improves the performance of photon management [2], [31], [32]. INZ materials provide a concrete implementation of this general principle. They accomplish effective angular concentration by using internal small phase spaces instead of bulk components such as lenses. As a result, they are much easier to integrate to accommodate diverse cell geometries. Similarly, INZ materials can also be used to improve the performance of other optoelectronic devices that require strong light-matter interactions, such as photodetectors and modulators.

Reference

[1] M. L. Brongersma, Y. Cui, and S. Fan, “Light management for photovoltaics using high-index nanostructures,” *Nat. Mater.*, vol. 13, no. 5, pp. 451–460, May 2014.

[2] E. Yablonovitch, “Statistical ray optics,” *J. Opt. Soc. Am.*, vol. 72, no. 7, p. 899, Jul. 1982.

[3] Z. Yu, A. Raman, and S. Fan, “Fundamental limit of nanophotonic light trapping in solar cells,” *Proc. Natl. Acad. Sci.*, vol. 107, no. 41, pp. 17491–17496, Oct. 2010.

[4] D. M. Callahan, J. N. Munday, and H. A. Atwater, “Solar Cell Light Trapping beyond the Ray Optic Limit,” *Nano Lett.*, vol. 12, no. 1, pp. 214–218, Jan. 2012.

[5] A. Alù, M. G. Silveirinha, A. Salandrino, and N. Engheta, “Epsilon-near-zero metamaterials and electromagnetic sources: Tailoring the radiation phase pattern,” *Phys. Rev. B*, vol. 75, no. 15, p. 155410, Apr. 2007.

[6] S. Vassant *et al.*, “Epsilon-Near-Zero Mode for Active Optoelectronic Devices,” *Phys. Rev. Lett.*, vol. 109, no. 23, p. 237401, Dec. 2012.

[7] N. Engheta, “Pursuing Near-Zero Response,” *Science*, vol. 340, no. 6130, pp. 286–287, Apr. 2013.

[8] R. Maas, J. Parsons, N. Engheta, and A. Polman, “Experimental realization of an epsilon-near-zero metamaterial at visible wavelengths,” *Nat. Photonics*, vol. 7, no. 11, pp. 907–912, Nov. 2013.

[9] P. Moitra, Y. Yang, Z. Anderson, I. I. Kravchenko, D. P. Briggs, and J. Valentine, “Realization of an all-dielectric zero-index optical metamaterial,” *Nat. Photonics*, vol. 7, no. 10, pp. 791–795, Oct. 2013.

[10] S. Molesky, C. J. Dewalt, and Z. Jacob, “High temperature epsilon-near-zero and epsilon-near-pole metamaterial emitters for thermophotovoltaics,” *Opt. Express*, vol. 21, no. S1, p. A96, Jan. 2013.

[11] A. A. Basharin, C. Mavidis, M. Kafesaki, E. N. Economou, and C. M. Soukoulis, “Epsilon near zero based phenomena in metamaterials,” *Phys. Rev. B*, vol. 87, no. 15, p. 155130, Apr. 2013.

[12] J. Luo *et al.*, “Arbitrary Control of Electromagnetic Flux in Inhomogeneous Anisotropic Media with Near-Zero Index,” *Phys. Rev. Lett.*, vol. 112, no. 7, p. 073903, Feb. 2014.

[13] Y. Xu and H. Chen, “Total reflection and transmission by epsilon-near-zero metamaterials with defects,” *Appl. Phys. Lett.*, vol. 98, no. 11, p. 113501, Mar. 2011.

[14] L.-Y. Zheng, Y. Wu, X. Ni, Z.-G. Chen, M.-H. Lu, and Y.-F. Chen, “Acoustic cloaking by a near-zero-index phononic crystal,” *Appl. Phys. Lett.*, vol. 104, no. 16, p. 161904, Apr. 2014.

[15] M. Silveirinha and N. Engheta, “Tunneling of Electromagnetic Energy through Subwavelength Channels and Bends using $\ensuremath{\epsilon}$-Near-Zero Materials,” *Phys. Rev. Lett.*, vol. 97, no. 15, p. 157403, Oct. 2006.

[16] B. Edwards, A. Alù, M. E. Young, M. Silveirinha, and N. Engheta, “Experimental Verification of Epsilon-Near-Zero Metamaterial Coupling and Energy Squeezing Using a Microwave Waveguide,” *Phys. Rev. Lett.*, vol. 100, no. 3, p. 033903, Jan. 2008.

[17] X. Huang, Y. Lai, Z. H. Hang, H. Zheng, and C. T. Chan, “Dirac cones induced by accidental degeneracy in photonic crystals and zero-refractive-index materials,” *Nat. Mater.*, vol. 10, no. 8, pp. 582–586, Aug. 2011.

[18] M. Zhou, L. Shi, J. Zi, and Z. Yu, “Extraordinarily Large Optical Cross Section for Localized Single Nanoresonator,” *Phys. Rev. Lett.*, vol. 115, no. 2, p. 023903, Jul. 2015.

[19] W. Shockley and H. J. Queisser, “Detailed Balance Limit of Efficiency of p-n Junction Solar Cells,” *J. Appl. Phys.*, vol. 32, no. 3, pp. 510–519, Mar. 1961.

[20] Z. Yu, A. Raman, and S. Fan, “Fundamental limit of light trapping in grating structures,” *Opt. Express*, vol. 18, no. S3, p. A366, Sep. 2010.

[21] V. Liu and S. Fan, “S4 : A free electromagnetic solver for layered periodic structures,” *Comput. Phys. Commun.*, vol. 183, no. 10, pp. 2233–2244, Oct. 2012.

[22] O. D. Miller, E. Yablonovitch, and S. R. Kurtz, “Strong Internal and External Luminescence as Solar Cells Approach the Shockley #x2013;Queisser Limit,” *IEEE J. Photovolt.*, vol. 2, no. 3, pp. 303–311, Jul. 2012.

[23] A. Niv, M. Gharghi, C. Gladden, O. D. Miller, and X. Zhang, “Near-Field Electromagnetic Theory for Thin Solar Cells,” *Phys. Rev. Lett.*, vol. 109, no. 13, p. 138701, Sep. 2012.

[24] J. N. Munday, “The effect of photonic bandgap materials on the Shockley-Queisser limit,” *J. Appl. Phys.*, vol. 112, no. 6, p. 064501, Sep. 2012.

[25] S. Sandhu, Z. Yu, and S. Fan, “Detailed balance analysis of nanophotonic solar cells,” *Opt. Express*, vol. 21, no. 1, p. 1209, Jan. 2013.

[26] Y. Li *et al.*, “On-chip zero-index metamaterials,” *Nat. Photonics*, vol. 9, no. 11, pp. 738–742, Nov. 2015.

[27] S. Campione, M. Albani, and F. Capolino, “Complex modes and near-zero permittivity in 3D arrays of plasmonic nanoshells: loss compensation using gain [Invited],” *Opt. Mater. Express*, vol. 1, no. 6, p. 1077, Oct. 2011.

[28] L. Sun, X. Yang, and J. Gao, “Loss-compensated broadband epsilon-near-zero metamaterials with gain media,” *Appl. Phys. Lett.*, vol. 103, no. 20, p. 201109, Nov. 2013.

[29] L. Sun and K. W. Yu, “Strategy for designing broadband epsilon-near-zero metamaterials,” *J. Opt. Soc. Am. B*, vol. 29, no. 5, p. 984, May 2012.

[30] L. Sun, J. Gao, and X. Yang, “Broadband epsilon-near-zero metamaterials with steplike metal-dielectric multilayer structures,” *Phys. Rev. B*, vol. 87, no. 16, p. 165134, Apr. 2013.

[31] Z. Yu, A. Raman, and S. Fan, “Nanophotonic light-trapping theory for solar cells,” *Appl. Phys. A*, vol. 105, no. 2, pp. 329–339, Sep. 2011.

[32] E. D. Kosten, J. H. Atwater, J. Parsons, A. Polman, and H. A. Atwater, “Highly efficient GaAs solar cells by limiting light emission angle,” *Light Sci. Appl.*, vol. 2, no. 1, p. e45, Jan. 2013.

CHAPTER FOUR

SPECTRAL SENSING IN NANOPHOTONIC STRUCTURES

4.1 Introduction

Two of the most popular approaches for spectral sensing are monochromators and Fourier transform interferometers. Both require delicate instruments, which limit their use in low-cost applications and tough environments. The key limitation of these methods comes from the fact a long optical path is required to distinguish lights of slightly different wavelengths. Having a long optical path in the free space requires bulky instruments to maintain the alignment. An alternative way to achieve a long optical path in a compact dimension is to have light bounce back and forward many times between interfaces on an integrated optical chip. For example, optical resonators with high quality factors, where light path is enhanced by millions of times compared to the geometrical sizes of the resonators, have been used for spectral sensing [1], [2]. However, the operation range is significantly limited by the number of resonators. Here we show a new method of spectral analysis based on the combination of compressive sensing [3] and nanophotonic structures, such as photonic crystal slabs [4]. Nanostructures with their abundant interfaces create much-enhanced optical paths, which is critical to achieve high spectral resolution. More importantly, unlike high-quality resonators whose spectral response consists of discrete narrow lines, the spectral responses of nanostructures are much more random with diverse features due to complex interferences. Such complex responses make it ideal to apply

compressive sensing for efficient signal recovery. Using this multiplex method, the operational range is much expanded compared to the high-Q resonator method. These nanostructures can be easily fabricated on a chip and therefore can potentially lead to low-cost, high resolution and compact spectrometers.

Before introducing our method, a general mathematical description is used first to briefly review conventional methods for spectral sensing. Considering an unknown signal light $I(\omega)$ passing through a spectral sensing instrument, whose response function can be described as $R(\omega,\rho)$. Here ρ is used to indicate a particular state of the instrument. A photodetector is used to measure the intensity of transmitted or reflected light d(ρ) as

$$d(\rho) = \int \mathrm{I}(\omega) R(\omega, \rho)\, d\omega \tag{4.1}$$

Many measurements need to be performed while the instrument is tuned to different states ρ. The measurement $d(\rho)$ can be understood as a transformation of signal $I(\omega)$. The recovery of signal $I(\omega)$ is done through an inverse transformation of the function $d(\rho)$. Different spectral sensing methods use different response functions and accordingly different transformation methods.

A monochromator uses a narrow-band filter based on a highly dispersive optical element, such as grating or prism (Fig. 4.1(a)). It separates lights of different wavelengths into different directions. A slit is used to selectively let through a narrow band of light around a central frequency ρ. The response function of an ideal monochromator is a delta function (Fig. 4.1(d))

$$\mathrm{R}(\omega, \rho) = \delta(\omega - \rho) \tag{4.2}$$

Using Eqs. (4.1) and (4.2), we have $d(\rho) = I(\rho)$. By measuring the intensity of transmitted light at each frequency ρ, the full spectrum can be obtained directly without an inverse

transformation. The resolution of this method scales with the length between the grating and the slit. Since the detector only receives a small portion of signal's energy at each measurement, the noise of detector has a great impact on the performance, making it difficult for infrared regime where the noise of detectors is typically large.

The Fourier transform interferometer (FTIR) has complete different response functions. The signal light is split into two different paths and then is combined (Fig. 4.1(b)). Because of the interference, $R(\omega,\rho)$ becomes sinusoidal with respect to the frequency (Fig. 4.1(e)):

$$R(\omega,\rho) = \frac{1+\cos(\rho\omega)}{2} \tag{4.3}$$

where ρ is the time delay between two optical paths of the interferometer. Measurements obtained by using different time delay are equivalent to a Fourier transformation of the signal:

$$d(\rho) = \int \frac{1}{2} \mathrm{I}(\omega)(1+\cos(\rho\omega))d\omega \tag{4.4}$$

The signal can be recovered through an inverse Fourier transformation. For each measurement, significant part of the signal's energy is sent to the detector. Comparing to monochromator, FTIR has the Fellgett advantage with a better signal-to-noise ratio for infrared light detection [5]. Similar to the monochromator method, the interferometer method also relies on a long and well-aligned optical path, again making it difficult to reduce the footprint without significantly sacrificing the performance.

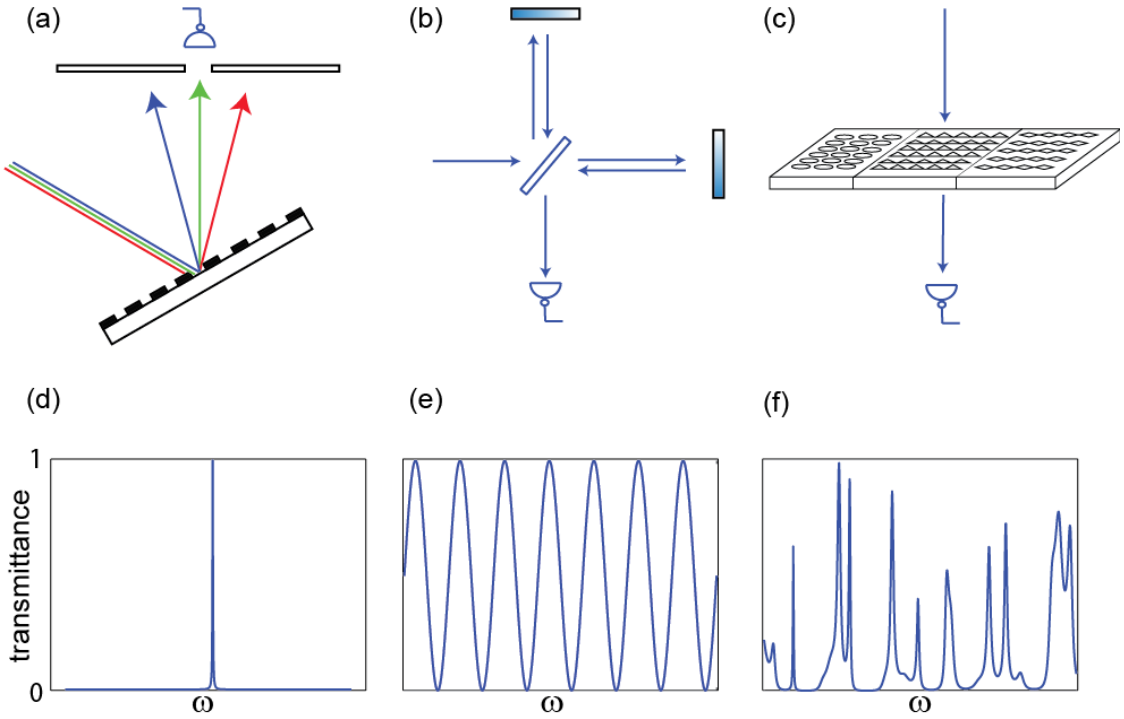

Fig. 4.1 (a) Monochromator based on grating. (b) Fourier transform interferometer. (c) Compressive sensing using nanophotonic structures. (d), (e), (f) are response functions for (a), (b), (c), respectively.

In this chapter, a spectral sensing method is proposed based on a completely different type of response function, which are obtained by passing the light through a set of different nanophotonic structures (Fig. 4.1(c)). The transmission and reflection spectra have randomly distributed spectral features (Fig. 4.1(f)), created by multiple reflections at interfaces of the nanostructure. Response functions at different states ρ are obtained by using different nanophotonic structures and are completely different from each other. They serve as the random bases used in compressive sensing. Before we further describe how to implement nanophotonic

structures to generate such random response functions, we first describe the procedure of compressive sensing algorism that will be used to recover the signal *I(ω)* from the measurement *d(ρ)*.

4.2 Spectral Sensing based on Compressive Sensing

In compressive sensing, the unknown signal is measured by projecting it to random bases. Typically, the number of measurements is smaller than the dimension of the unknown signal, which requires the signal to be recovered by finding solutions to an underdetermined linear system. It is particularly powerful for recovering sparse signals using less number of measurements than what the Nyquist-Shannon sampling theorem requires. Compressive sensing has been used for advanced imaging [6-12]. Here the basis pursuit method described in l_1-magic program for compressive signal recovery is used[13].

To apply the compressive sensing algorism, all continuous spectral functions are digitized. The spectrum of the signal light is converted to a *N*-dimension vector $I_n = I(\omega_n)$, , $n = 1, \dots, N$. The random bases, i.e. the response functions of nanostructures, are digitized as $R_{m,n} = R(\omega_n, \rho_m)$ where $m = 1, \dots, M$, representing *M* different states of ρ, i.e. *M* different photonic structures. The measurement is then expressed as. Eq. (4.1) is converted to a set of linear equations with *N* unknowns and *M* equations

$$\vec{d} = \overleftrightarrow{R}\vec{I} \tag{4.5}$$

It is always desirable to digitalize the unknown signal with a large *N* for fine resolution. Therefore, for the cases $N > M$, the linear equations are underdetermined. The unknown $\vec{I}$ can be recovered by solving a convex program known as the basis pursuit [14]

$$(P_1)\ \ \min\|I\|_1\ \ \text{subject to}\ \vec{d} = \overleftrightarrow{R}\vec{I} \tag{4.6}$$

where $\|I\|_1 = \sum |I_n|$ is the l_1 norm of the vector.

Here I want to emphasize that the performance of compressive sensing relies on the randomness of the measuring bases. Therefore, response functions should have diverse spectral features with both broad and narrow line shapes. In addition, different response functions should have minimal correlation. This requirement is difficult to be achieved using conventional interferometers consisting of bulk mirrors, lenses or gratings. On the other hand, complex interferences in nanostructures offer extremely rich amount of spectral features. More importantly, the enormous degrees of freedom in choosing the spatial parameters of the nanostructures allow us to create virtually unlimited number of different response functions.

4.3 Signal Recovery Results in Simulation

Next, simulations are performed for a particular example to demonstrate the signal recovery based on compressive sensing. The nanophotonic structure consists of a photonic crystal slab (Fig. 4.2(a)). It has four layers from the top to the bottom: a 1 μm thick Si layer, a 2.5 μm thick SiO_2 layer, a 0.3 μm thick Si layer and a SiO_2 substrate. A periodic lattice of air holes with a radius r = 0.9 μm are patterned in the top Si layer. The lattice constants in two orthogonal directions are p_1 = 3 μm and p_2 = 3.2 μm. The reflection spectrum (Fig. 4.2(b)) consists of diverse spectral features. Specifically, the vertical interfaces of air holes cause light to bounce in the lateral direction parallel to the slab. Such lateral propagation forms guided resonances [15], which greatly enhances the optical path with extremely high quality factors. In addition, the slab also has multiple interfaces along the direction normal to the slab. Light bounces between these

interfaces, forming Fabry-Perot (FP) resonances. While these FP resonances do not have high quality factors, they play a unique role in enhancing the diversity of spectral features through Fano interference [16]. Fano interference is a result of the interference between guided resonance and direct background transmission. Unlike the symmetrical Lorentz response in regular optical cavities, Fano interference creates highly asymmetrical lineshapes [17], [18]. The specific lineshapes depend on the phase and transmittance of the background transmission, which is modulated by the FP resonances. The combination of high-Q guided resonances and low-Q FP resonances through Fano interference leads to diverse spectral features.

A signal light in the spectral range from 1450 nm to 1550 nm is analyzed. The spectrum is digitalized with 0.1 nm resolution, represented by N = 1001 unknowns to be determined. M = 400 different photonic crystal slabs are used by varying the radius of the holes and the lattice constants. The measurement consists of first passing signal light through each photonic crystal slab and then recording the reflected or transmitted intensity with a photodetector.

These 400 structures have the same layer configuration but with different lattice structures. They are divided into two categories: rectangular and triangular lattices. Different combinations of hole sizes and lattice constants are used to obtain different structures and response functions. p_1 varies from 3 μm to 4 μm with a 0.1 μm step. For a given p_1 value, p_2 varies from p_1 to 4 μm with a 0.2 μm step. The diameter of holes ranges from 1.4 μm to p_1 - 1 μm with a 0.2 μm step. The reflection spectra are obtained by solving the Maxwell's equations using rigorous coupled-wave analysis (RCWA). The simulations were performed with *S4* program [19]. A representative spectrum is shown in Fig. 4.2(b).

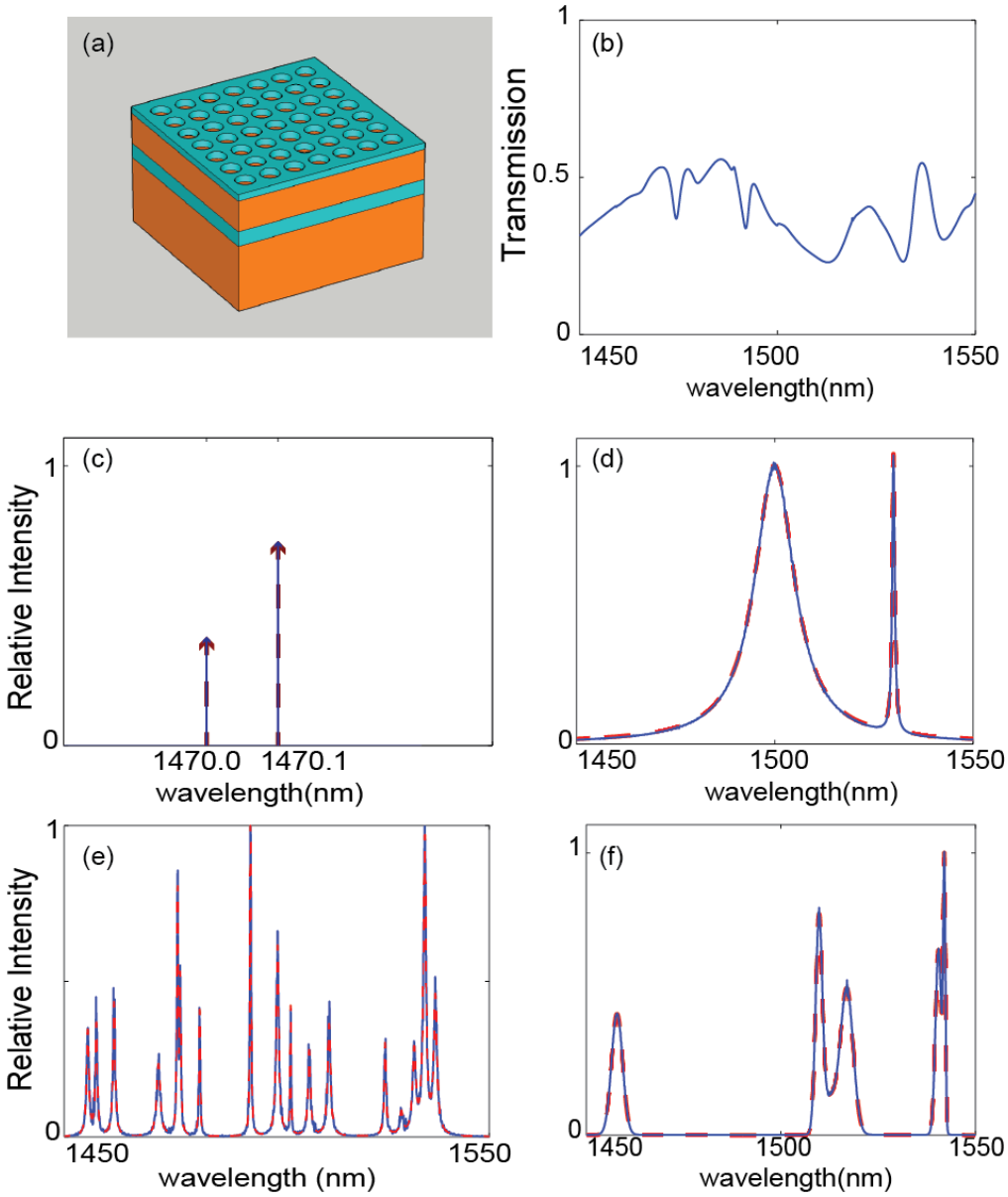

Fig. 4.2 (a) Structure of photonic crystal slab. (b) Representative reflection spectrum. (c) – (f) Simulated signal recovery using compressive sensing algorithm and response functions of photonic crystal slabs for (c) two discrete spikes (d) two Lorentzian lines (e) multiple Lorentzian lines (f) five Gaussian lines. The recovered signals (blue solid lines) agree well with the original (red dashed lines).

To evaluate the performance, a random signal is generated and the measurement processes are simulated using Eq. (4.1). The signal is recovered by feeding $d(\rho)$ into the compressive sensing program implemented in l_1-magic [13]. First, a signal consisting of a few continuous waves of different wavelengths is used. The spectrum consists of a few sharp spikes. Such a signal is used to evaluate the resolution. The distance between the frequencies of two continuous waves is 0.1 nm (as shown in Fig. 4.2(c)). Both the spectral position and the intensity of the signal are recovered well. The resolution is maximized when the spectral features of the response functions are sufficiently complex within certain frequency range. To improve the complexity of the spectra, the optical path length can be enhanced by increasing the number of structural interfaces and the thickness of the structures. For example, by increasing the thickness of top layer photonic crystal slab, or using two layers of different photonic crystal slabs, the resolution can be further improved. In addition, the number of response functions, the sparsity of the signal, and measurement noise also affect the resolution, as expected for any compressive sensing method. The second test signal consists of a broadband Lorentz signal with a 30 nm bandwidth and a sharp peak on it. The third test signal combines 17 Lorentzian lines and the fourth combines 5 Gaussian lines. In all cases (Fig. 4.2(d), 4.2(e), 4.2(f)), the original signals are recovered with high fidelity.

Even though a large number of different photonic crystal slabs are used, these structures can be readily integrated on a chip. For visible and near-infrared spectral sensing, the required feature sizes can be readily defined by photolithography. The entire chip containing hundreds of different photonic crystal slabs can be as small as a few millimeters. The response functions of these nanostructures will be measured in the calibration process. Unknown signals can then be

projected onto the chip and the measurement can be taken in parallel by an array of photodetectors. Alternatively, for weak signals, the measurement can be done sequentially as shown in Fig. 4.1(c).

4.4 Discussion

In additional to photonic crystal slabs, other nanostructures with complex interferences can also be used to generate random spectral features. For example, multilayer structures with layer thickness ranging from hundreds of nanometers to a few micrometers can generate complex and fine spectral features (Fig. 4.3).

It is desirable to have minimal correlation among different response functions for the best performance of compressive sensing. Next, I will use the multilayer structure as an example to evaluate the impact of correlation. I compare two types of multilayer structures, both consisting of 5 layers of silicon slabs with air spacing. For the first type (Fig. 4.3(a)), all 5 layers have the same thicknesses of 15 μm. Different response functions are obtained by randomly varying the thicknesses of air spacing between layers in the range from 3 – 4 μm. Fig. 4.3(b) – (e) show three representative spectra. By examining these spectra, it's recognized that despite different detailed features, they all share a common pattern with a spectral periodicity determined by the FP resonance of the 15 μm thick Si slab. I can evaluate the correlation among different spectral response defined as

$$C_{i,j} = \frac{E\left[\left(R(\omega,\rho_i)-E(R(\omega,\rho_i))\right)\left(R(\omega,\rho_j)-E\left(R(\omega,\rho_j)\right)\right)\right]}{\sqrt{E\left[\left(R(\omega,\rho_i)-E(R(\omega,\rho_i))\right)^2\right]E\left[\left(R(\omega,\rho_j)-E\left(R(\omega,\rho_j)\right)\right)^2\right]}} \tag{4.7}$$

where E(.) represents the average. The response functions ae obtained by simulating 400 different structures using S4 [19]. The average correlation is 0.74, indicating significant similarity among different response functions. Using this set of response functions, the compressive sensing algorithm is applied for a signal consisting of 5 Lorentzian peaks (Fig. 4.3(e), red line). The peak positions and heights are barely recovered (Fig. 4.3(e), blue line).

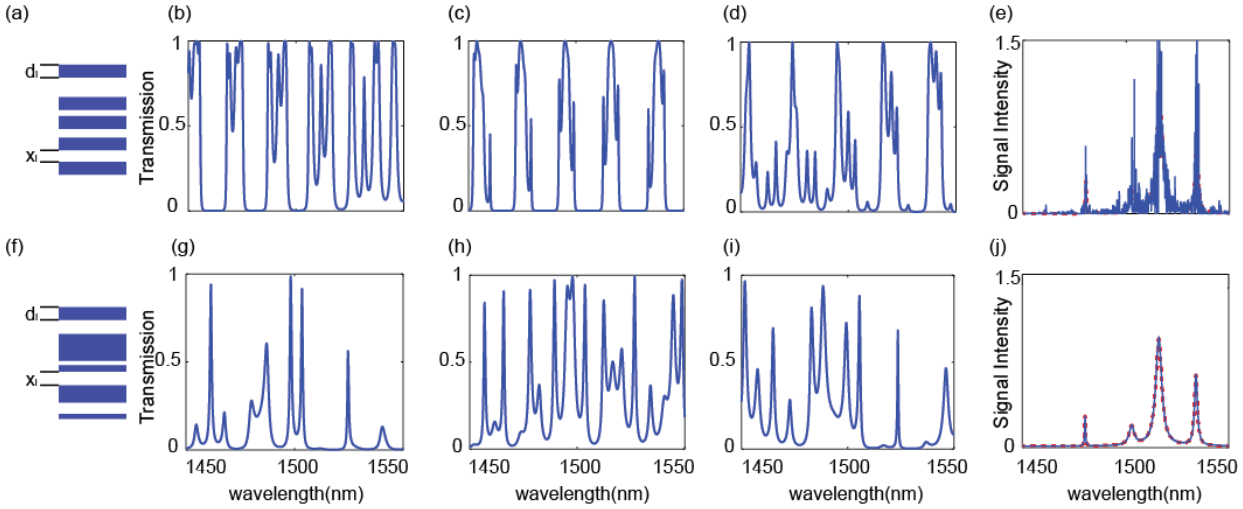

Fig. 4.3 The performance of the signal recovery depends on the implementation of the response functions. (a) The multi-layer structure that generates the response functions have 5 Si layers (blue slabs) with the same thickness of 15 μm. The distances are varied to obtain 400 different structures. (b) – (d) Three representative response functions. (e) The recovered signal barely reproduces the original signal with a high noise level. (f) Both the thicknesses and the distances between layers are varied. (g) – (i) Three representative response functions for (f). (j) the recovered signal agrees well with the original signal.

For the second type of structures (Fig. 4.3(f)), 400 different response functions are obtained by changing both the thickness of and the spacing between Si layers. The spacing is randomly

chosen between 3 to 4 μm and the thickness is randomly chosen between 10 nm to 15 μm. Fig. 4.3(g) - (i) show representative spectra. The average correlation for 400 different response functions is 0.01, much smaller than that of the first type of structures. Fig. 4.3(j) shows that the same signal now is very well recovered by this set of response functions. The comparison between these two types of structures shows the importance of correlation in designing photonic structures.

Finally, the second type of multi-layer structure is used to evaluate the tolerance of measurement noise. Noise is inevitable in every step of experimental measurement. In the simulation, a random noise is added to the response functions. This noise could come from the experimental measurement of the response functions during the initial calibration of the instrument. Specifically,

$$R'(\omega,\rho) = R(\omega,\rho) + \delta R(\omega,\rho) \tag{4.8}$$

where $R(\omega,\rho)$ is the true response function and $R'(\omega,\rho)$ is the measured response function. $\delta R(\omega,\rho)$ is the random noise. The measurement of the signal passing through the photonic structure also induces a noise given by

$$d'(\rho) = \int \mathrm{I}(\omega) R(\omega,\rho)\, d\omega + \delta d(\rho) \tag{4.9}$$

$I'(\omega)$ is recovered by compressive sensing algorithm using measured data $R'(\omega,\rho)$ and $d'(\rho)$. Fig. 4.4(a) shows the case without noise. Fig. 4.4(b) shows the noisy case with a signal-to-noise ratio of 40dB, e.g. the ratios between δR and R and between δd and d. In both cases, $I'(\omega)$ (blue solid line) agrees well with $I(\omega)$ (red dashed line).

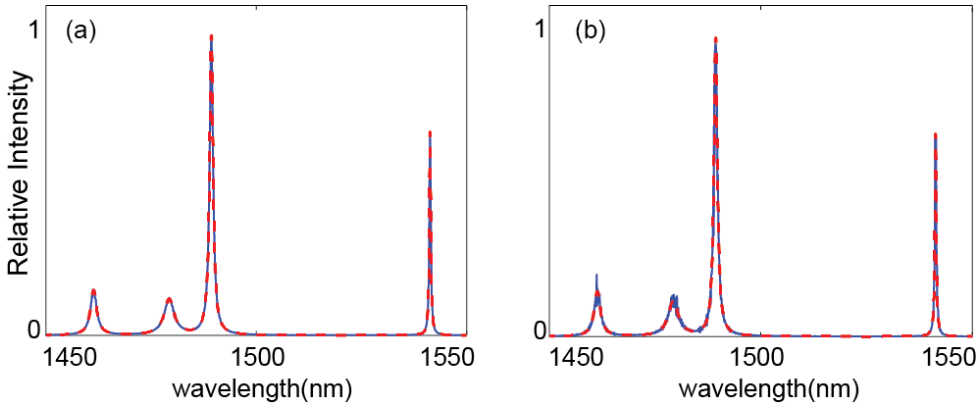

Fig. 4.4 Result of signal recovery using compressive sensing without noise (a) and with noise (b). Red dashed lines are the original signals, and blue solid lines are the recovered signals.

4.5 Conclusion

In conclusion, this chapter shows a method of spectral analysis based on compressive sensing. Nanophotonic structures are used to generate random sensing bases. Simulations show that such method could achieve very high resolution with good tolerance of noise. It can be potentially implemented in a very compact dimension to be used in low-cost applications.

Reference

[1] X. Gan, N. Pervez, I. Kymissis, F. Hatami, and D. Englund, “A high-resolution spectrometer based on a compact planar two dimensional photonic crystal cavity array,” *Appl. Phys. Lett.*, vol. 100, no. 23, p. 231104, 2012.

[2] Z. Xia *et al.*, “High resolution on-chip spectroscopy based on miniaturized microdonut resonators,” *Opt. Express*, vol. 19, no. 13, pp. 12356–12364, 2011.

[3] E. J. Candes, J. Romberg, and T. Tao, “Robust uncertainty principles: exact signal reconstruction from highly incomplete frequency information,” *IEEE Trans. Inf. Theory*, vol. 52, no. 2, pp. 489–509, Feb. 2006.

[4] S. G. Johnson, S. Fan, P. R. Villeneuve, J. D. Joannopoulos, and L. A. Kolodziejski, “Guided modes in photonic crystal slabs,” *Phys. Rev. B*, vol. 60, no. 8, p. 5751, 1999.

[5] P. B. Fellgett, *The Theory of Infrared Sensitivities and Its Application to Investigations of Stellar Radiation in the Near Infra-red*. 1951.

[6] M. F. Duarte *et al.*, “Single-pixel imaging via compressive sampling,” *IEEE Signal Process. Mag.*, vol. 25, no. 2, pp. 83–91, Mar. 2008.

[7] L. Zhu, W. Zhang, D. Elnatan, and B. Huang, “Faster STORM using compressed sensing,” *Nat. Methods*, vol. 9, no. 7, pp. 721–723, Jul. 2012.

[8] C. M. Watts *et al.*, “Terahertz compressive imaging with metamaterial spatial light modulators,” *Nat. Photonics*, vol. 8, no. 8, pp. 605–609, Aug. 2014.

[9] O. Katz, Y. Bromberg, and Y. Silberberg, “Compressive ghost imaging,” *Appl. Phys. Lett.*, vol. 95, no. 13, p. 131110, Sep. 2009.

[10] W. L. Chan, K. Charan, D. Takhar, K. F. Kelly, R. G. Baraniuk, and D. M. Mittleman, "A single-pixel terahertz imaging system based on compressed sensing," *Appl. Phys. Lett.*, vol. 93, no. 12, p. 121105, Sep. 2008.

[11] A. Shabani *et al.*, "Efficient measurement of quantum dynamics via compressive sensing," *Phys. Rev. Lett.*, vol. 106, no. 10, Mar. 2011.

[12] A. Szameit *et al.*, "Sparsity-based single-shot subwavelength coherent diffractive imaging," *Nat. Mater.*, vol. 11, no. 5, pp. 455–459, May 2012.

[13] *l1_magic*. Available: http://statweb.stanford.edu/~candes/l1magic/. [Accessed: 10-Jul-2014].

[14] E. J. Candes and T. Tao, "Decoding by Linear Programming," *IEEE Trans. Inf. Theory*, vol. 51, no. 12, pp. 4203–4215, Dec. 2005.

[15] S. G. Johnson, S. Fan, P. R. Villeneuve, J. D. Joannopoulos, and L. A. Kolodziejski, "Guided modes in photonic crystal slabs," *Phys. Rev. B*, vol. 60, no. 8, p. 5751, 1999.

[16] S. Fan, W. Suh, and J. D. Joannopoulos, "Temporal coupled-mode theory for the Fano resonance in optical resonators," *JOSA A*, vol. 20, no. 3, pp. 569–572, 2003.

[17] S. Fan, "Sharp asymmetric line shapes in side-coupled waveguide-cavity systems," *Appl. Phys. Lett.*, vol. 80, no. 6, p. 908, 2002.

[18] C. Wu *et al.*, "Fano-resonant asymmetric metamaterials for ultrasensitive spectroscopy and identification of molecular monolayers," *Nat. Mater.*, vol. 11, no. 1, pp. 69–75, Nov. 2011.

[19] V. Liu and S. Fan, "S4 : A free electromagnetic solver for layered periodic structures," *Comput. Phys. Commun.*, vol. 183, no. 10, pp. 2233–2244, Oct. 2012.

CHAPTER FIVE

ON-CHIP MICRO-SPECTROMETER BASED ON PHOTONIC CRYSTAL SLAB

5.1 Introduction

Spectrometers are widely used for spectral analysis to study light-matter interactions [1], [2]. Current designs for spectrometers generally fall into two categories: the first one is based on a direct measuring method where individual bands are measured separately after introducing temporal or spatial band separations [3], [4] . As bands are measured separately, the incident power of the detector for each measurement is relatively low. In order to increasing the signal to noise ratio for the cases when the detector noise dominant, another spectral sensing method based on multiplexing principle is used. In multiplexing, instead of measuring individual band separately, multiple bands are encoded and measured at the same time [5], [6]. In other words, the unknown signal is encoded in each measurement with a different encoding mask. The measured results carry information of multiple bands with different weights. After several measurements, all the measurement results form a 'barcode' that could uniquely identify the original signal using some computational reconstruction method.

Based on these two methods, sophisticated free-space spectrometers such as monochromator and FTIR are widely used. Despite their outstanding performance, their applications are limited by the size and cost. In recent years a lot of efforts are invested in the development of cheap, portable and easy to use systems. Micro-spectrometers based on dispersive elements such as

planar waveguide spectrometers [7]–[9] require relatively large footprint to achieve high resolution. This is because in order to distinguish light with slightly different wavelength, light has to travel a long distance to accumulate phase difference until it's detectable. Alternatively, micro-spectrometers based on resonant devices are developed [10]–[12]. Due to resonance, the optical path length is greatly enhanced thus higher resolution could be achieved in a small footprint. However, the free spectral range is limited by the number of resonators used. In addition, these devices are sensitive to fabrication errors. Multiplexing based devices such as quantum dot spectrometers are not CMOS-compatible [13], resulting in a complex and expensive fabrication process.

This chapter proposed a CMOS-compatible micro-spectrometer based on photonic crystal slab. The typical structure of a photonic crystal slab consists of a dielectric slab with periodic structures, such as an array of air holes on top. As light could be bounced back and forward many times among the abundant interfaces, millions times longer optical path length could be achieved compared to the geometrical size of the structure. In addition, the proposed device requires no fiber or waveguide to couple signals in, which makes it a great candidate for serving as individual spectral pixels in snapshot hyperspectral imaging.

5.2 Micro-Spectrometer Design

As shown in Fig. 5.1, the designed micro-spectrometer consists of 6×6 different photonic crystal structures. Each of these structures has a different transmission spectrum with each other. This is achieved by tuning the pattern shape, size and lattice constant. The slab is then integrated on top of a Complementary Metal–Oxide–Semiconductor (CMOS) sensor array.

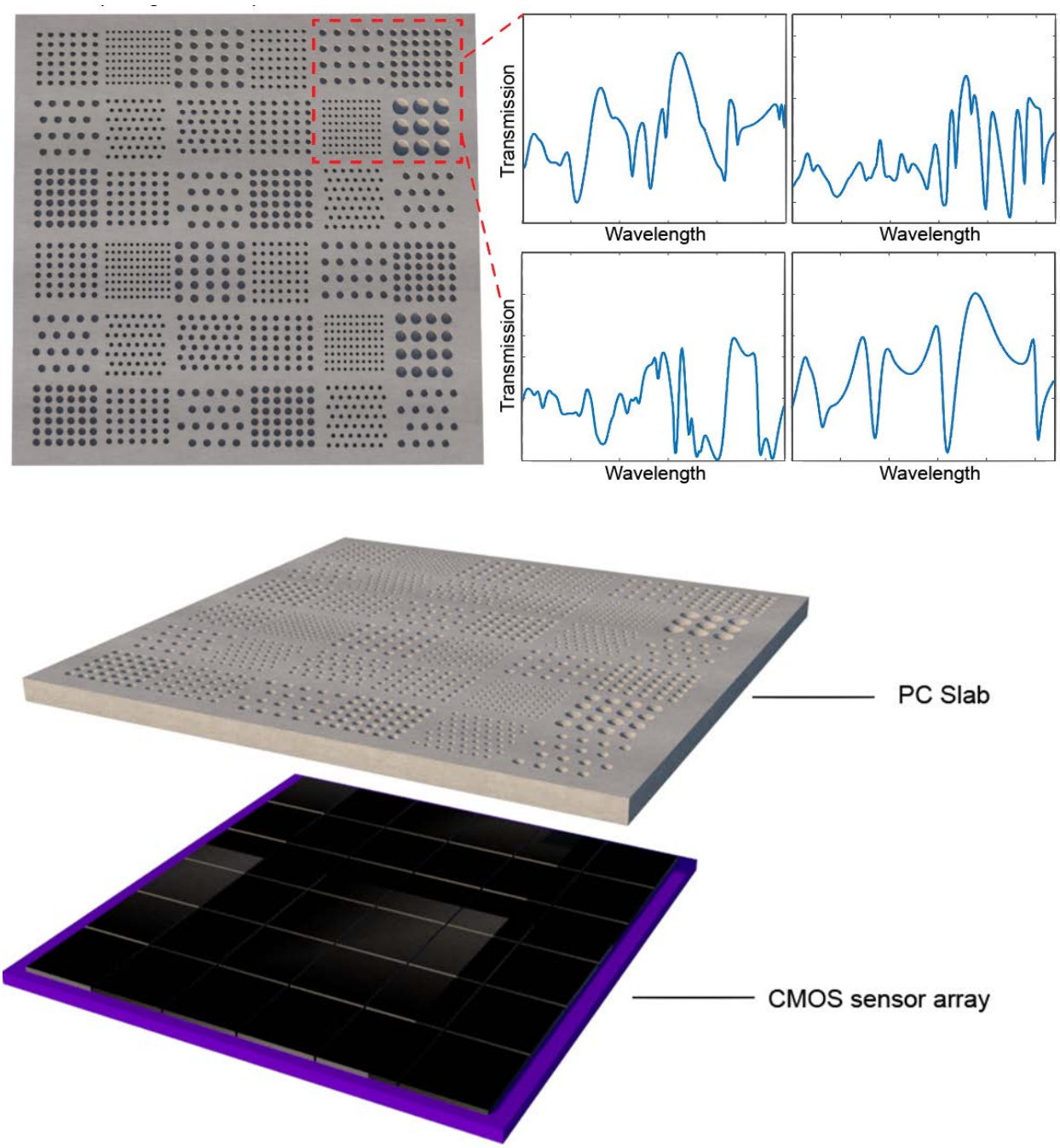

Fig. 5.1 Schematic of the designed micro-spectrometer. A PC slab consisting of 6 × 6 different nanostructures is integrated on top of a CMOS sensor array. The transmission spectrum for each of the structure is different with each other.

When measuring a spectrum, the unknown signal can be simply projected onto all the 6×6 structures without fiber coupling required, as shown in Fig. 5.2. The transmitted intensity of the unknown signal through each of the structure is collected from the CMOS sensor array. Based on the transmitted intensity distribution, the original signal could be obtained by computational reconstruction methods such as linear regression [14], [15] or compressive sensing [16]. In other words, the transmitted intensity distribution works as a 'fingerprint' that uniquely identifies the incident signal.

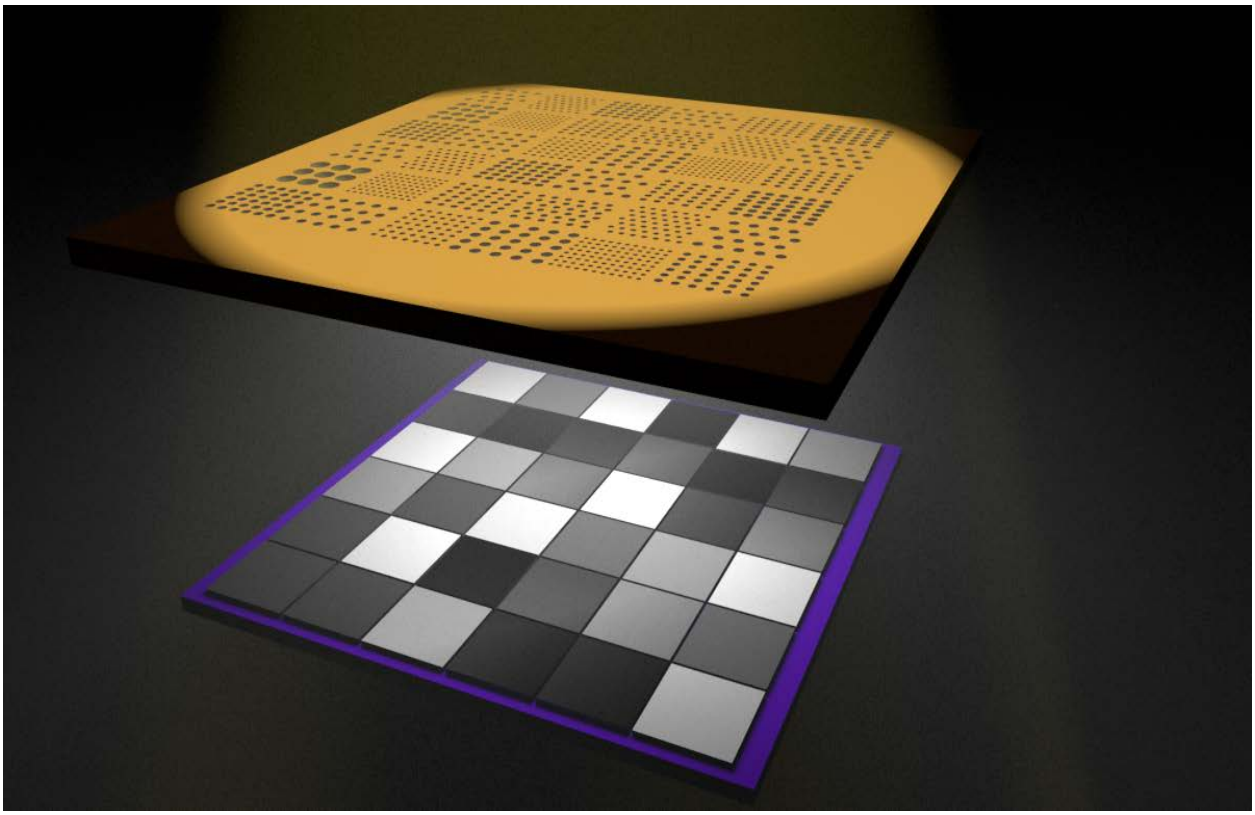

Fig. 5.2 Spectral analysis process using the designed device. The unknown signal is projected directly onto the 6×6 structures, and the transmitted intensity of the unknown signal through each of the structure is then collected from the CMOS sensor array.

Mathematically, the incident unknown spectrum $I(\lambda)$ is discretized into a *N*-dimension vector $I_n = I(\lambda_n), n = 1, \dots, N$. The transmitted intensity of the unknown spectrum through the m^{th} PC structure D_m can be written as:

$$D_m = \sum_1^N I(\lambda_n) T_m(\lambda_n),\ m = 1,2, \dots, M \tag{5.1}$$

Where $T_m(\lambda)$ is the transmission spectrum of the m^{th} PC structure, which is predetermined in the calibration process by sweeping the wavelength from λ_1 to λ_N and taking the ratio of the incident light intensity with and without the device for each λ_n. With *M* structures equation (5.1) is turned into *M* linear equations with *N* unknowns

$$D = TI \tag{5.2}$$

Where *D* is a single column with the *M* measured transmitted intensity, *T* is a $M \times N$ coding matrix with the m^{th} row corresponds to the transmission spectrum of the m^{th} PC structure. The input spectra *I* can then be recovered by minimizing the l_2 norm

$$\|D - TI\|_2^2 \quad \text{subject to } \mathrm{I}_n > 0 \tag{5.3}$$

In practice, *D* is subject to experimental noise, then a smooth signal *I* that approximates *D* can be reconstructed as a solution to a regularized objective function

$$\min_I \|D - TI\|_2^2 + \mathrm{k}\|SI\|_2^2 \quad \text{subject to } \mathrm{I}_n > 0 \tag{5.4}$$

Where $k > 0$ is the weight. SI is the second-order difference of the signal *I*. Minimizing $\|SI\|_2^2$ forces *I* to be smooth.

5.3 Experimental Demonstration

To experimentally demonstrate the proposed device, a micro-spectrometer is designed and fabricated. This device consists of an array of 6×6 different PC structures on a 500nm-thick

Silicon on Sapphire (SOS) substrate (Fig. 5.3(a)). As shown in the scanning electron microscope (SEM) images in Fig. 5.3(b), each PC structure with a fixed size of 32μm × 32μm consists of a periodic lattice of air holes. In order to achieve different transmission spectrums for the 6 × 6 structures, we have the flexibility to tune the diameter of the air holes, lattice constants in two dimensions, as well as the angle between them. For our designed micro-spectrometer targeted at the spectral range from 550 nm – 750 nm, the diameters of the air holes are chosen from 100 nm – 400 nm, the lattice constants in each dimension vary from 300 nm – 500 nm, and the angle between them varies from 30° – 90°. The air holes were patterned using electron-beam lithography and etched down 150 nm with reactive ion beam etching. The measured transmission spectrums *T* for four different structures are shown in Fig. 5.3(c), which confirms that by tuning the parameters of photonic structures, different transmission spectrums are achieved. Incident signal is encoded by different transmission spectrums when passing through the device and recorded by a CMOS sensor array (Thorlabs, DCC3260M). Fig. 5.3(d) shows two examples of the captured images by the CMOS sensor array when exposed to two different signals, which proved that there's one-to-one mapping between the incident signal and the transmitted intensity distribution collected on the CMOS sensor array. Each captured image delivers information to uniquely identify the original signal using computational reconstruction methods such as linear regression described by Eq. (5.4).

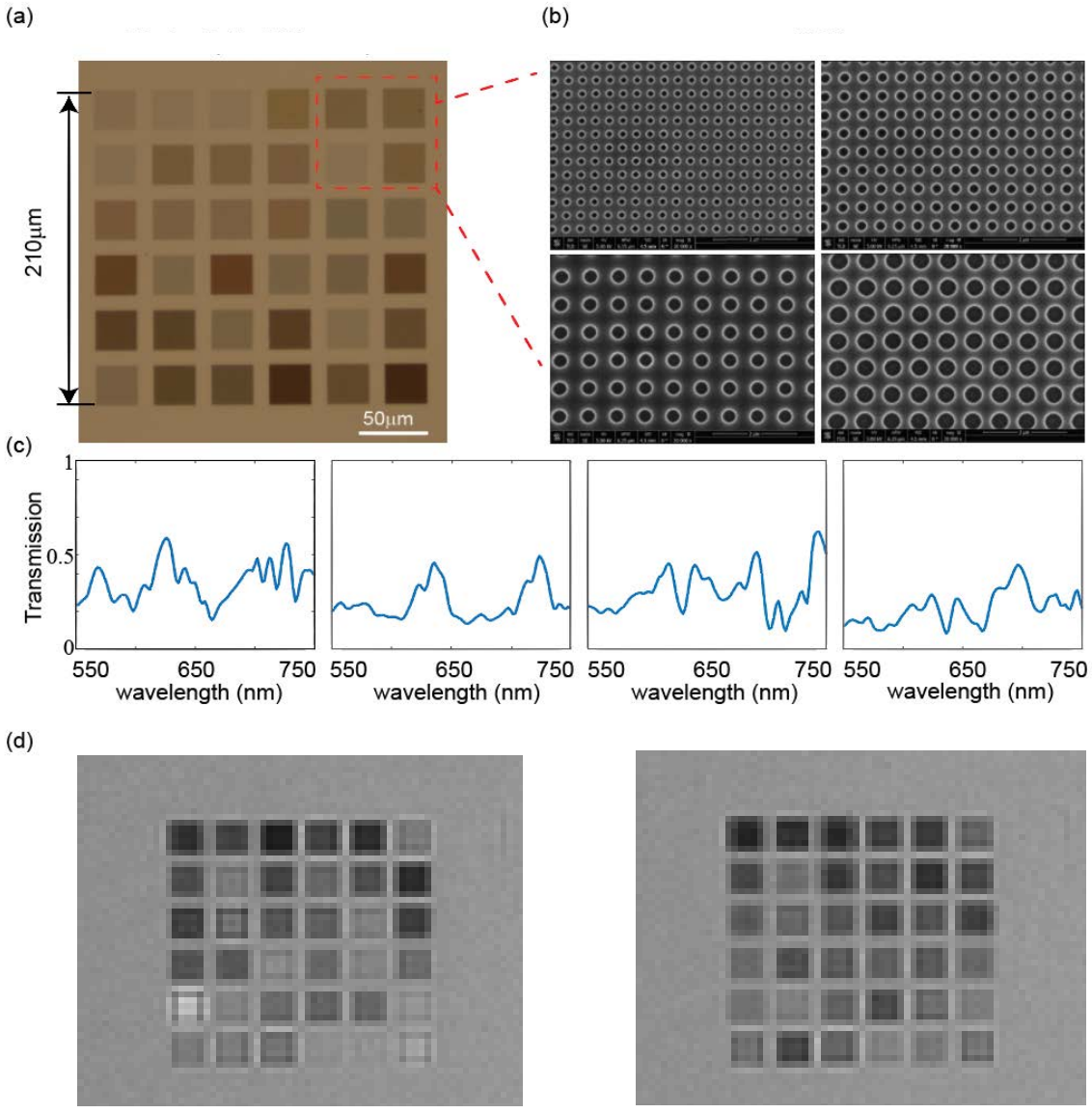

Fig. 5.3 (a) Fabricated device under microscope. (b) Four different PC structures under SEM. (c) Measured transmission spectrums for four different PC structures. (d) Transmitted intensity distribution measured by the CMOS sensor array when illuminated at 610 nm (left) and 650 nm (right).

The performance of the PC slab based spectrometer is tested by measuring several arbitrary spectra with varying intensity and bandwidth, and comparing the results with the reference spectra measured by a commercial monochromator. Signals being measured are generated by a random combination of a white light source with a set of filters and several LEDs. Spectrums with single peaks are targeted first. As shown by Fig. 5.4, the measurement results matches well with the references. Then some random signals with multiple peaks and varying intensity and bandwidth are tested. The results are shown by Fig. 5.5, where all the major features are successfully recovered.

To demonstrate the resolution of the micro-spectrometer, The device obtained accurate spectra of a series of narrow lines with 1 nm peak-to-peak separation (generated by a monochromator) across the 200 nm spectral range (Fig. 5.6(a) – (b)). As a further resolution test, the spectrometer resolved a closely positioned double peak separated by 2 nm (Fig. 5.6(c)). The double peak spectrum is synthesized by adding the intensity recorded separately on the detectors for each of the two sharp spectral lines passing through the spectrometer. This confirms that the abundant interfaces of the PC structures greatly enhances the optical length path and enable 1-2 nm resolution with a ~210 μm × 210 μm device size. Resolution and signal recovery accuracy could be improved by adding more PC structures, using more sophisticated recovery algorithms, increasing calibration resolution and reducing measurement error.

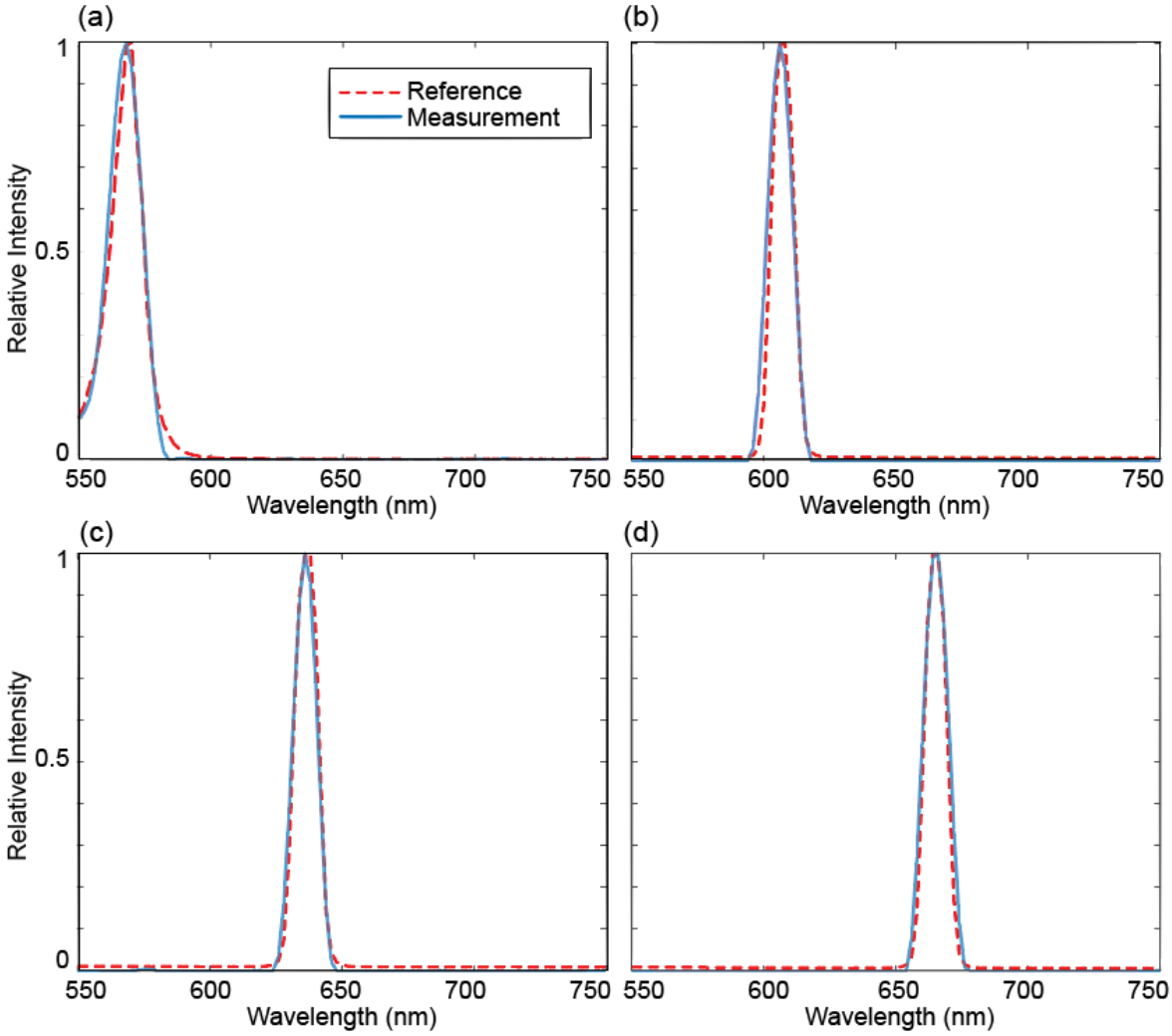

Fig. 5.4 Measurement results for signals with single peak. (a) Emission spectrum of a 570 nm LED with 14 nm bandwidth. (b)-(d) Spectrum generated by a combintaion of a white light source and a bandpass filter with 10 nm bandwidth at (b) 610 nm. (c) 640 nm. (d) 670 nm. The measured signals (blue solid lines) agree well with the reference (red dashed lines).

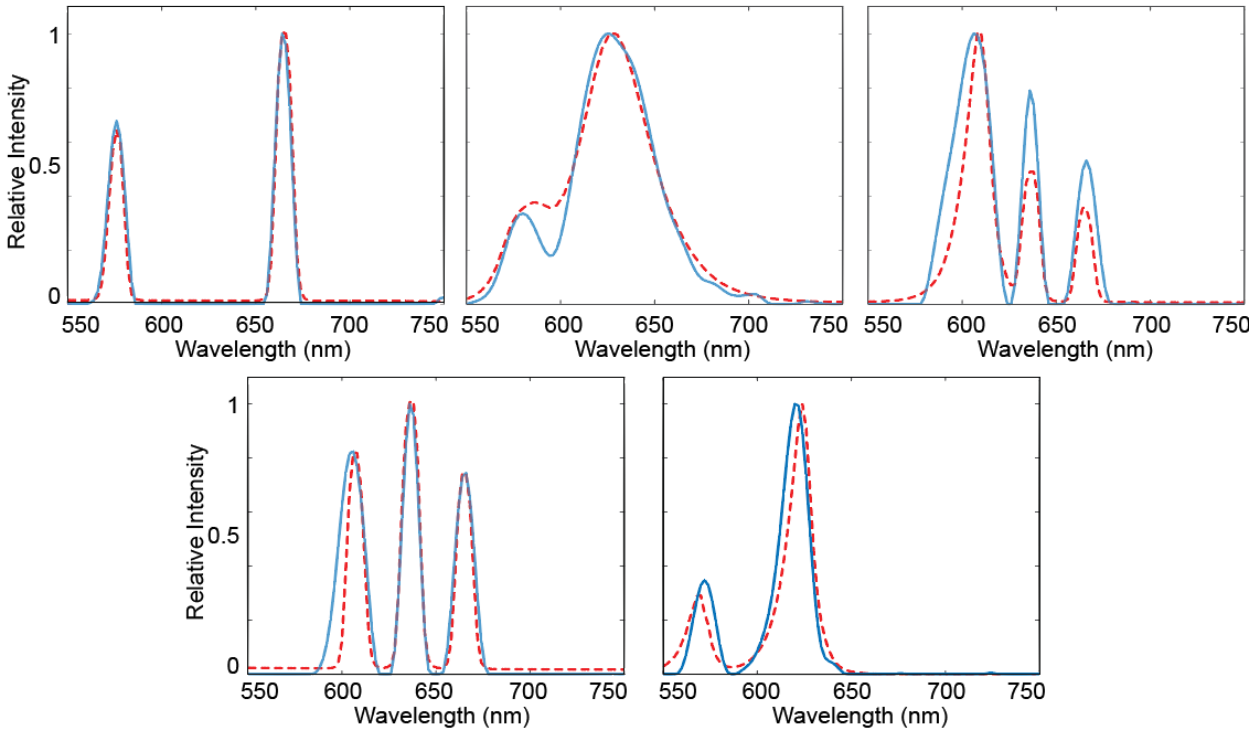

Fig. 5.5 Measurement results for random signals with variying bandwidth and intensity. The measured signals (blue solid lines) agree well with the reference (red dashed lines).

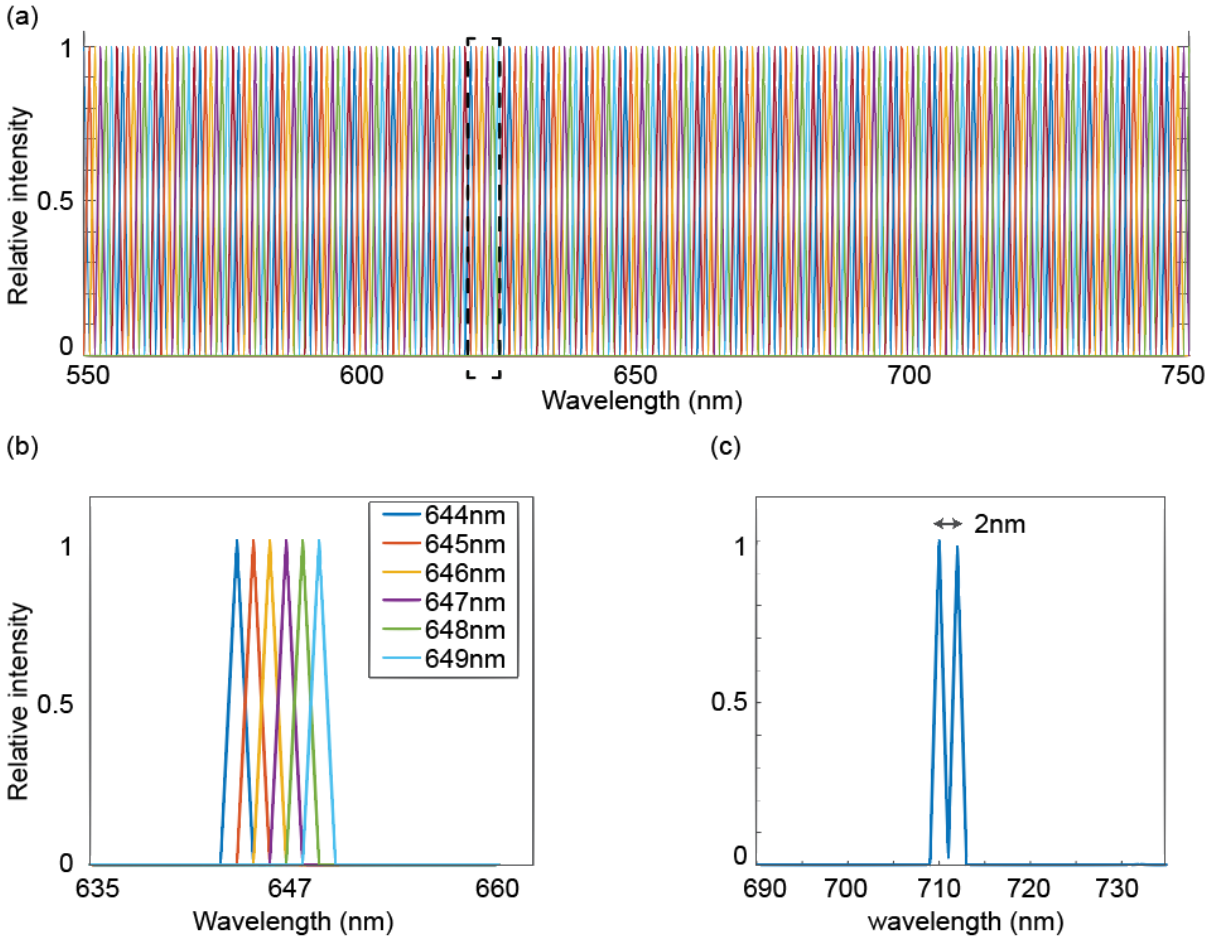

Fig. 5.6 (a) A series of sharp peaks across the 200 nm spectral range with 1 nm peak-to-peak distance obtained by the PC slab based micro-spectrometer (b) Circled part in (a). (c) Resolved double peak spectrum with 2 nm separation.

As the designed device is compact with relatively high resolution, easy to fabricate with low cost and can capture spectral information in a snapshot fashion, it has the great potential in the fields that require spectral sensing such as bioscience, chemistry or material analysis. To demonstrate one of its applications, Fig. 5.7 shows a case when two different spectral signals are perceived the same by human eyes or RGB cameras, a phenomenon referred to as metamerism [17]. Metamerism prevents the unique recovery of spectra directly from the response of any photoreceptor made following the Principle of Univariance [18] in color imaging. In contrast, our device could clearly distinguish the two signals and reconstruct the exact spectral components for each.

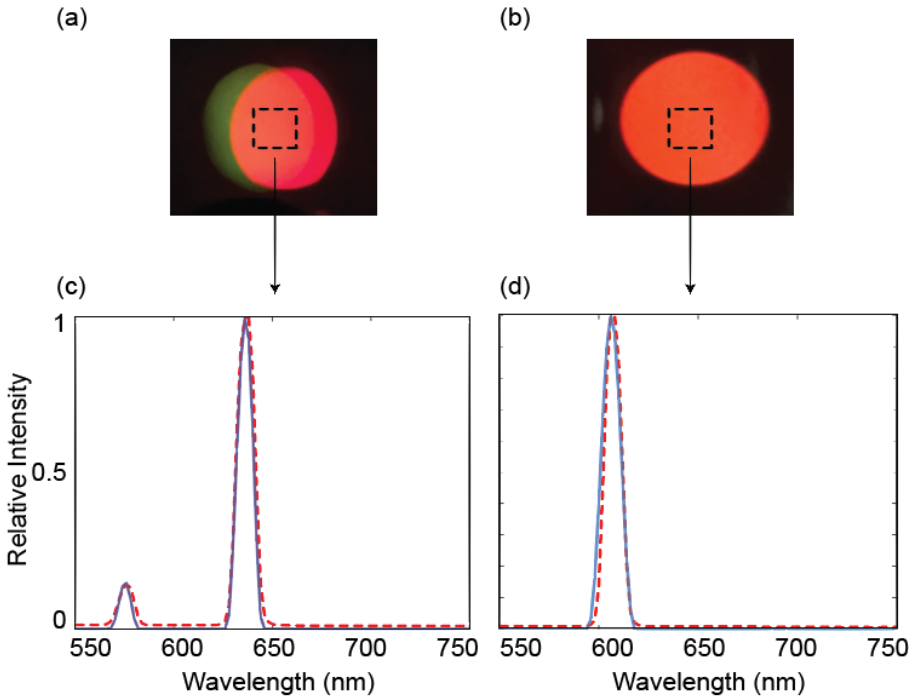

Fig. 5.7 A case when two different spectrums are perceived the same by an RGB camera while the spectral information could be accurately obtained by the designed device. (a) An orange

color mixed by green and red. (b) A pure orange color, which is perceived the same with the one shown in (a) by an RGB camera. (c) – (d) Spectral information obtained by the PC slab based spectrometer for (a) and (b). The measurement results (blue solid lines) agree well with the reference measured by a commercial monochromator (red dashed lines).

5.4 Application in Snapshot Hyperspectral Imaging

I next demonstrate another potential application of the micro-spectrometer in spectral imaging. When imaging a scene, a spectral imager could produce a spatial map that indicates the spectral variation (x, y, λ) in order to identifying materials or finding objects [19]. Generally used spectral imaging techniques include spatial scanning [20], [21], which acquires the spectral information of the scene point by point, and spectral scanning [21], which captures a series of monochromatic spatial maps of the scene. As the scanning methods require stationary measuring system, long acquisition time and are only accurate for non-moving scene, non-scanning methods have been developed over the years, which could yield the full date cube (x, y, λ) via a single measurement. A number of carefully designed systems have been proposed, such as integral field spectrometry with fiber bundles/lenslet arrays (IFS-F/IFS-L) [22]–[24], multispectral beam splitting (MSBS) [25], computed tomography imaging spectrometry (CTIS) [26], image replicating imaging spectrometers (IRIS) [27], coded aperture snapshot spectral imager (CASSI) [28], [29]. Most of these methods require precision alignment and manufacturing costs are high. Alternatively, we propose a snapshot multispectral imaging camera based on our designed micro-spectrometer which is easy to use, compact and low cost.

As the micro-spectrometer requires neither disperser nor waveguide or fiber to couple signals

into the structures, it's easy to be integrated. This fundamental advantage opens up the possibility for it to serve as individual pixels of a snapshot hyperspectral imaging camera by simply attaching an array of micro-spectrometers to a commercial photodetector array. To illustrate this idea, we fabricated 10 ×10 identical micro-spectrometers on a SOS substrate with the same design and fabrication process with before (Fig. 5.8). Each micro-spectrometer serves as a spectral pixel and captures the spectral information of the part of an image that is projected onto it, and the process is in parallel over all pixels. In other words, the spatial and spectral information are acquired separately. The fabricated device is then attached onto the chip of a CMOS camera, enabling a 10 ×10 pixel snapshot hyperspectral camera with ~210μm × 210μm pixel size. The active region spans ~2.1mm × 2.1mm. Notice that the current design of the hyperspectral camera is for demonstration purpose, in practice more pixels could be added efficiently by fabricating the micro-spectrometer array using high resolution photolithography. For example, a ~170 × 110 micro-spectrometer array can be integrated on a 8688 × 5792 pixel CMOS camera with 4.14μm × 4.14μm pixel size (Canon, EOS 5DS). To further increase the spatial resolution, the size of each micro-spectrometer could be made smaller by reducing the number of periods for each PC structure, which is a tradeoff between the spatial resolution and single pixel performance.

Before the camera is used for spectral imaging, same calibration process for individual micro-spectrometer is performed by measuring the transmission spectrum of each PC structure with sweeping monochromatic light at 2 nm steps in the range 550 nm – 750 nm. The hyperspectral camera is then tested by taking the image of some characters on a paper (Fig. 5.9(a)) with a 35mm lens (Fujinon, CF35HA-1) attached. As a first test we targeted a single number 5

illuminated at 600 nm $\pm$ 1 nm (FWHM). Fig. 5.9(b) shows the captured image by the spectral camera which records the optical intensity distribution of the image of number 5 that has passed through each PC structure of the 10×10 micro-spectrometers. Again, due to spectral multiplexing, this image itself can't be associated with any specific wavelength. Instead, computational methods should be performed based on the intensity distribution recorded for each micro-spectrometer. Fig. 5.9(c) shows the obtained spectral information for this number 5 from a particular pixel. Fig. 5.9(d) - (f) displays three images from the reconstructed data cube at 570 nm, 600 nm, 630 nm. Both the spatial and spectral information are accurately obtained. As only a small number of spectral pixels are available, the ones that are partially illuminated are turned off manually.

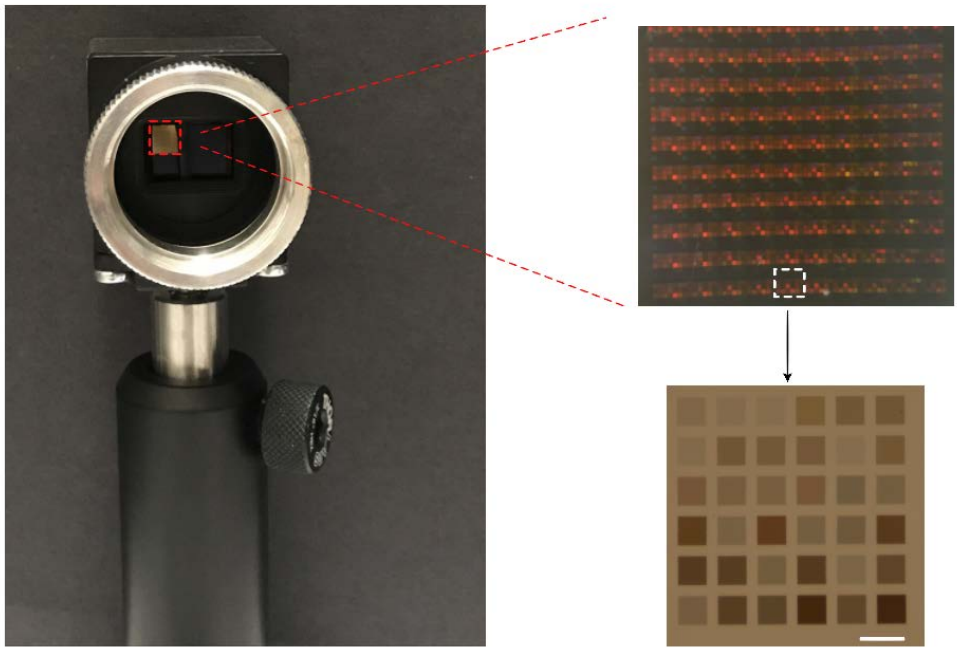

Fig. 5.8 Image of the spectral camera, where a chip with 10×10 identical micro-spectrometers is attached onto a CMOS camera. Scale Bar: 50 μm.

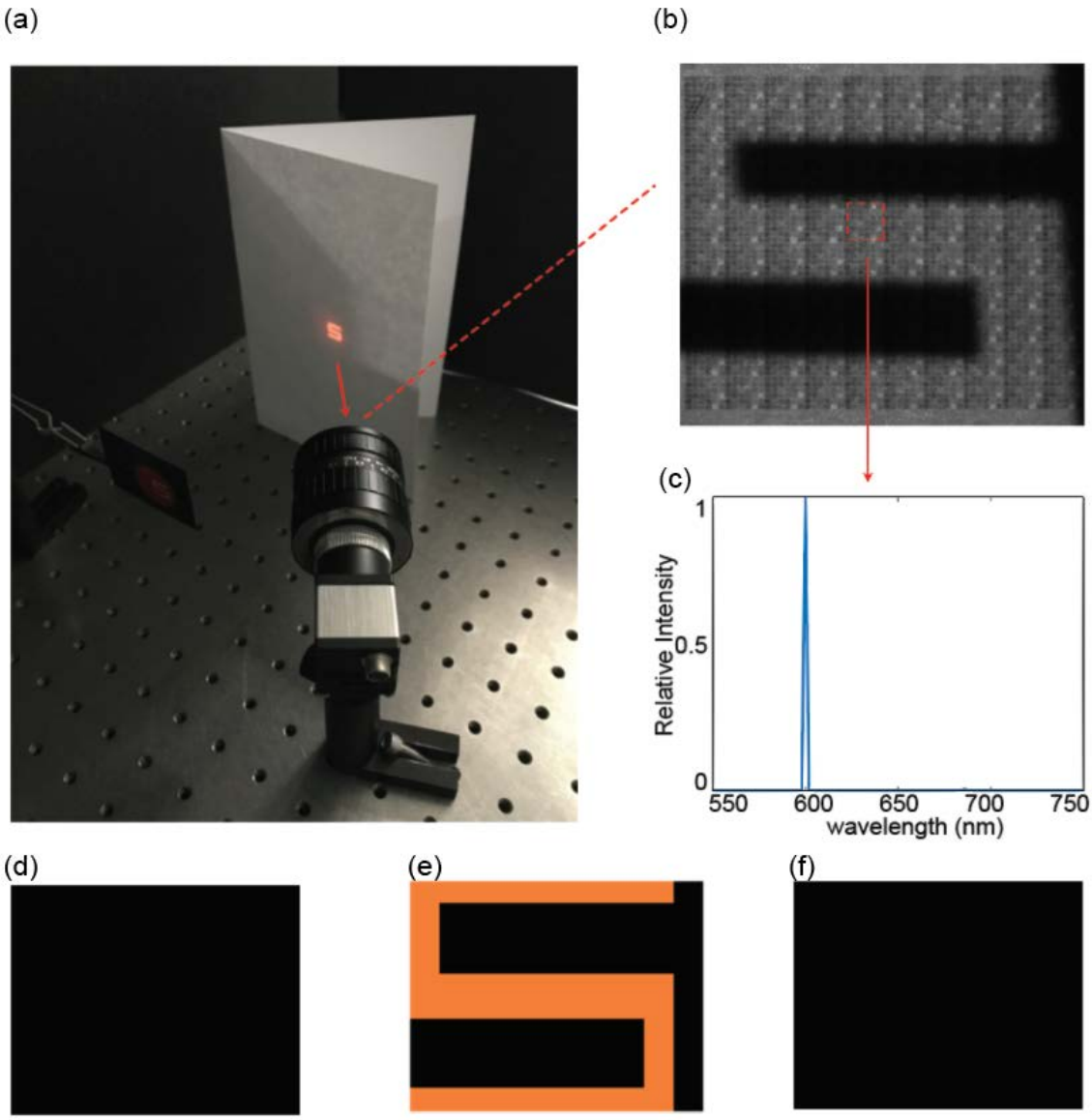

Fig. 5.9 (a) Optical setup for taking the images of some characters on the paper using the designed hyperspectral camera. (b) Image taken by the CMOS camera for a number 5 on the paper illuminated at 600 nm. (c) Spectral information obtained by a particular spectral pixel. (d) – (f) The spatial maps from the reconstructed data cube at 570 nm, 600 nm, 630 nm, respectively.

I next consider a character formed by overlapping two numbers 5 and 9 on the paper (Fig. 5.10(a)), with number 5 illuminated at 610 $\pm$ 5 nm and number 9 illuminated at 670 $\pm$ 1 nm. The reconstructed spectral and spatial information of this character is demonstrated by Fig. 5.10(b)-(d) showing three images at 610 nm, 640 nm and 670 nm. The overlapped numbers are separated by wavelength difference, which an RGB camera is not capable of.

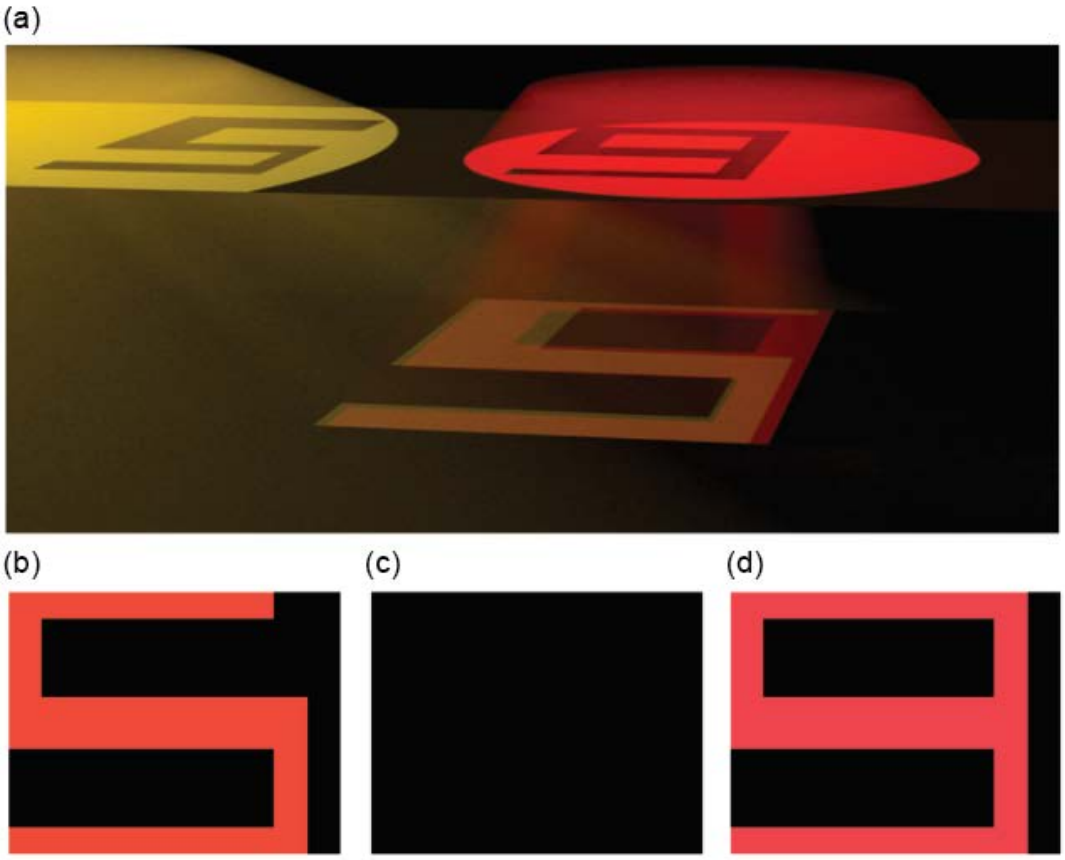

Fig. 5.10 (a) The image that's being analyzed by the designed hyperspectral camera, which is formed by overlapping two numbers, 5 and 9, with 5 illuminated at 610 nm and 9 illuminated at 670 nm. (b) – (d) The spatial map from the reconstructed data cube at 610 nm, 640 nm, 670 nm, respectively.

5.5 Conclusion

In summary, this chapter experimentally demonstrates a CMOS-compatible on-chip miro-spectrometer based on PC slab. As the optical path length is greatly enhanced by the abundant interfaces of the nanophotonic structures, the designed device could achieve high resolution in a compact size. In addition, the device could obtain spectral information with a snapshot fashion and no fiber coupling is necessary. This opens up the possibility for the PC based micro-spectrometer to serve as individual spectral pixels for snapshot hyperspectral imaging, which is low cost and easy to use.

Reference

[1] H. Ayvaz and L. E. Rodriguez-Saona, “Application of handheld and portable spectrometers for screening acrylamide content in commercial potato chips,” *Food Chem.*, vol. 174, pp. 154–162, May 2015.

[2] M. Wagner, D. Tonoli, E. Varesio, and G. Hopfgartner, “The use of mass spectrometry to analyze dried blood spots,” *Mass Spectrom. Rev.*, vol. 35, no. 3, pp. 361–438, Jun. 2016.

[3] E. K. Plyler and L. R. Blaine, “Infrared high-resolution grating spectrometer,” *J. Res. Natl. Bur. Stand.*, vol. 62, no. 1, p. 7, Jan. 1959.

[4] PRISM Collaboration *et al.*, “PRISM (Polarized Radiation Imaging and Spectroscopy Mission): An Extended White Paper,” *J. Cosmol. Astropart. Phys.*, vol. 2014, no. 02, pp. 006–006, Feb. 2014.

[5] W. D. Perkins, “Fourier transform-infrared spectroscopy: Part l. Instrumentation,” *J. Chem. Educ.*, vol. 63, no. 1, p. A5, Jan. 1986.

[6] E. D. Nelson and M. L. Fredman, “Hadamard Spectroscopy,” *JOSA*, vol. 60, no. 12, pp. 1664–1669, Dec. 1970.

[7] X. J. M. Leijtens, B. Kuhlow, and M. K. Smit, “Arrayed Waveguide Gratings,” in *Wavelength Filters in Fibre Optics*, vol. 123, H. Venghaus, Ed. Springer Berlin Heidelberg, 2006, pp. 125–187.

[8] A. J. Lowery, “Design of arrayed-waveguide grating routers for use as optical OFDM demultiplexers,” *Opt. Express*, vol. 18, no. 13, pp. 14129–14143, Jun. 2010.

[9] J. Chen, Y. Yang, and N. Zhu, “Echelle grating based mode demultipexer for vertical mode-division multiplexing,” *Opt. Express*, vol. 24, no. 21, p. 24509, Oct. 2016.

[10] O. Painter, J. Vučkovič, and A. Scherer, “Defect modes of a two-dimensional photonic crystal in an optically thin dielectric slab,” *J. Opt. Soc. Am. B*, vol. 16, no. 2, p. 275, Feb. 1999.

[11] Z. Xia *et al.*, “High resolution on-chip spectroscopy based on miniaturized microdonut resonators,” *Opt. Express*, vol. 19, no. 13, pp. 12356–12364, Jun. 2011.

[12] B. B. C. Kyotoku, L. Chen, and M. Lipson, “Sub-nm resolution cavity enhanced microspectrometer,” *Opt. Express*, vol. 18, no. 1, pp. 102–107, Jan. 2010.

[13] J. Bao and M. G. Bawendi, “A colloidal quantum dot spectrometer,” *Nature*, vol. 523, no. 7558, pp. 67–70, Jul. 2015.

[14] F. Nie, X. Cai, H. Huang, and C. Ding, “Efficient and Robust Feature Selection via Joint 2,1-Norms Minimization,” p. 9.

[15] S. R. Becker, E. J. Candès, and M. C. Grant, “Templates for convex cone problems with applications to sparse signal recovery,” *Math. Program. Comput.*, vol. 3, no. 3, pp. 165–218, Sep. 2011.

[16] E. J. Candes, J. Romberg, and T. Tao, “Robust uncertainty principles: exact signal reconstruction from highly incomplete frequency information,” *IEEE Trans. Inf. Theory*, vol. 52, no. 2, pp. 489–509, Feb. 2006.

[17] A. Akbarinia and K. R. Gegenfurtner, “Color metamerism and the structure of illuminant space,” *JOSA A*, vol. 35, no. 4, pp. B231–B238, Apr. 2018.

[18] W. A. H. Rushton, “Review Lecture. Pigments and signals in colour vision,” *J. Physiol.*, vol. 220, no. 3, pp. 1P-31P, Feb. 1972.

[19] C.-I. Chang, *Hyperspectral Imaging: Techniques for Spectral Detection and Classification*. Springer Science & Business Media, 2003.

[20] H.-T. Lim and V. M. Murukeshan, "Spatial-scanning hyperspectral imaging probe for bio-imaging applications," *Rev. Sci. Instrum.*, vol. 87, no. 3, p. 033707, Mar. 2016.

[21] H. Grahn and P. Geladi, *Techniques and Applications of Hyperspectral Image Analysis*. John Wiley & Sons, 2007.

[22] H. Jupnik, "Fiber Optics. Principles and Applications. N. S. Kapany. Academic Press, New York, 1967. 447 pp., illus. $17.50," *Science*, vol. 159, no. 3811, pp. 183–183, Jan. 1968.

[23] J. Bland-Hawthorn *et al.*, "Hexabundles: imaging fiber arrays for low-light astronomical applications," *Opt. Express*, vol. 19, no. 3, pp. 2649–2661, Jan. 2011.

[24] J. Meaburn, "Versatile nebular insect-eye fabry-perot spectrograph," *Appl. Opt.*, vol. 14, no. 2, pp. 465–469, Feb. 1975.

[25] T. C. George *et al.*, "Distinguishing modes of cell death using the ImageStream multispectral imaging flow cytometer," *Cytom. Part J. Int. Soc. Anal. Cytol.*, vol. 59, no. 2, pp. 237–245, Jun. 2004.

[26] T. Okamoto and I. Yamaguchi, "Simultaneous acquisition of spectral image information," *Opt. Lett.*, vol. 16, no. 16, pp. 1277–1279, Aug. 1991.

[27] A. R. Harvey and D. W. Fletcher-Holmes, "High-throughput snapshot spectral imaging in two dimensions," in *Spectral Imaging: Instrumentation, Applications, and Analysis II*, 2003, vol. 4959, pp. 46–55.

[28] A. A. Wagadarikar, N. P. Pitsianis, X. Sun, and D. J. Brady, “Video rate spectral imaging using a coded aperture snapshot spectral imager,” *Opt. Express*, vol. 17, no. 8, p. 6368, Apr. 2009.

[29] M. E. Gehm, R. John, D. J. Brady, R. M. Willett, and T. J. Schulz, “Single-shot compressive spectral imaging with a dual-disperser architecture,” *Opt. Express*, vol. 15, no. 21, pp. 14013–14027, Oct. 2007.